# 5

# Main physical phenomena used for particle detection and basic counter types

What we observe is not nature itself, but nature exposed to our method of questioning.

*Werner Heisenberg*

A particular type of detector does not necessarily make only one sort of measurement. For example, a segmented calorimeter can be used to determine particle tracks; however, the primary aim of such a detector is to measure the energy. The main aim of drift chambers is a measurement of particle trajectories but these devices are often used for particle identification by ionisation measurements. There is a number of such examples.

This chapter considers the main physical principles used for particle detection as well as the main types of counters (detector elements). The detectors intended for the measurement of certain particle characteristics are described in the next chapters. A brief introduction to different types of detectors can be found in [1].

## 5.1 Ionisation counters

### *5.1.1 Ionisation counters without amplification*

An *ionisation counter* is a gaseous detector which measures the amount of ionisation produced by a charged particle passing through the gas volume. Neutral particles can also be detected by this device via secondary charged particles resulting from the interaction of the primary ones with electrons or nuclei. Charged particles are measured by separating the charge-carrier pairs produced by their ionisation in an electric field and guiding the



https://doi.org/10.1017/9781009401531.008 Published online by Cambridge University Press

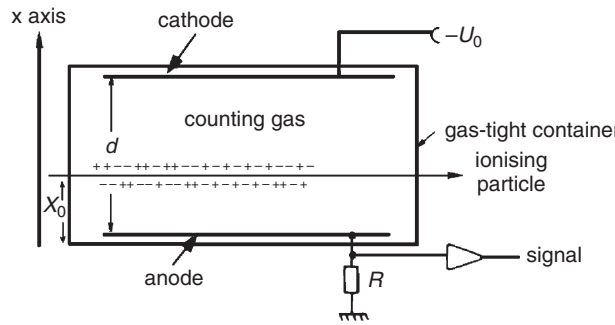


Fig. 5.1. Principle of operation of a planar ionisation chamber.

ionisation products to the anode or cathode, respectively, where corresponding signals can be recorded. If a particle is totally absorbed in an *ionisation chamber*, such a detector type measures its energy [2, 3].

In the simplest case an ionisation chamber consists of a pair of parallel electrodes mounted in a gas-tight container that is filled with a gas mixture which allows electron and ion drift. A voltage applied across the electrodes produces a homogeneous electric field.

In principle the counting gas can also be a liquid or even a solid (solid-state ionisation chamber). The essential properties of ionisation chambers are not changed by the phase of the counting medium.

Let us assume that a charged particle is incident parallel to the electrodes at a distance $x_0$ from the anode (Fig. 5.1). Depending on the particle type and energy, it produces along its track an ionisation, where the average energy required for the production of an electron–ion pair, $W$, is characteristic of the gas (see Table 1.2).

The voltage $U_0$ applied to the electrodes provides a uniform electric field

$$|\vec{E}| = E_x = U_0/d \ . \tag{5.1}$$

In the following we will assume that the produced charge is completely collected in the electric field and that there are no *secondary ionisation* processes or *electron capture* by possible electronegative gas admixtures.

The parallel electrodes of the ionisation chamber, acting as a capacitor with capacitance $C$, are initially charged to the voltage $U_0$. To simplify the consideration let us assume that the load resistor $R$ is very large so that the capacitor can be considered to be independent. Suppose $N$ charge-carrier pairs are produced along the particle track at a distance $x_0$ from the anode. The drifting charge carriers induce an electric charge on the electrodes which leads to certain change of the voltage, $\Delta U$. Thereby the

https://doi.org/10.1017/9781009401531.008 Published online by Cambridge University Press

stored energy $\frac{1}{2}CU_0^2$ will be reduced to $\frac{1}{2}CU^2$ according to the following equations:

$$\frac{1}{2}CU^2 = \frac{1}{2}CU_0^2 - N\int_{x_0}^{x} qE_x \,\mathrm{d}x \ , \tag{5.2}$$

$$\frac{1}{2}CU^2 - \frac{1}{2}CU_0^2 = \frac{1}{2}C(U+U_0)(U-U_0) = -N\cdot q\cdot E_x\cdot(x-x_0) \ . \tag{5.3}$$

The voltage drop, however, will be very small and one may approximate

$$U + U_0 \approx 2U_0 \ , \quad U - U_0 = \Delta U \ . \tag{5.4}$$

Using $E_x = U_0/d$ one can work out $\Delta U$ with the help of Eq. (5.3),

$$\Delta U = -\frac{N\cdot q}{C\cdot d}(x - x_0) \ . \tag{5.5}$$

The signal amplitude $\Delta U$ has contributions from fast-moving electrons and the slowly drifting ions. If $v^+$ and $v^-$ are the constant *drift velocities* of ions and electrons while $+e$ and $-e$ are their charges, one obtains

$$\begin{aligned} \Delta U^+ &= -\frac{Ne}{Cd}v^+\Delta t \ , \\ \Delta U^- &= -\frac{N(-e)}{Cd}(-v^-)\Delta t \ , \end{aligned} \tag{5.6}$$

where $\Delta t$ is the drift time. For ions $0 < \Delta t < T^+ = (d - x_0)/v^+$ while for electrons $0 < \Delta t < T^- = x_0/v^-$. It should be noted that electrons and ions cause contributions of the same sign since these carriers have opposite charges and opposite drift directions.

Because of $v^- \gg v^+$, the signal amplitude will initially rise linearly up to

$$\Delta U_1 = \frac{Ne}{Cd}\cdot(-x_0) \tag{5.7}$$

(the electrons will arrive at the anode, which is at $x = 0$, at the time $T^-$) and then will increase more slowly by the amount which originates from the movement of ions,

$$\Delta U_2 = -\frac{Ne}{Cd}(d - x_0) \ . \tag{5.8}$$

Therefore the total signal amplitude, that is reached at $t = T^+$, is

$$\Delta U = \Delta U_1 + \Delta U_2 = -\frac{Ne}{Cd}x_0 - \frac{Ne}{Cd}(d - x_0) = -\frac{N\cdot e}{C} \ . \tag{5.9}$$

https://doi.org/10.1017/9781009401531.008 Published online by Cambridge University Press

This result can also be derived from the equation describing the charge on a capacitor, $\Delta Q = -N \cdot e = C \cdot \Delta U$, which means that, independent of the construction of the ionisation chamber, the charge $Q$ on the capacitor is reduced by the collected ionisation $\Delta Q$, and this leads to a voltage amplitude of $\Delta U = \Delta Q/C$.

These considerations are only true if the charging resistor is infinitely large or, more precisely,

$$RC \gg T^-, T^+ \ . \tag{5.10}$$

When $RC \neq \infty$, expressions (5.6) should be modified,

$$\begin{aligned} \Delta U^+ &= -\frac{Ne}{d} v^+ R(1 - \mathrm{e}^{-\Delta t/RC}) \ , \\ \Delta U^- &= -\frac{N(-e)}{d}(-v^-) R(1 - \mathrm{e}^{-\Delta t/RC}) \ . \end{aligned} \tag{5.11}$$

In practical cases $RC$ is usually large compared to $T^-$, but smaller than $T^+$. In this case one obtains [4]

$$\Delta U = -\frac{Ne}{Cd} x_0 - \frac{Ne}{d} v^+ R(1 - \mathrm{e}^{-\Delta t/RC}) \ , \tag{5.12}$$

which reduces to Eq. (5.9) if $RC \gg T^+ = (d - x_0)/v^+$ .

For electric field strengths of 500 V/cm and typical drift velocities of $v^- = 5\,\mathrm{cm/\mu s}$, collection times for electrons of 2 µs and for ions of about 2 ms are obtained for a drift path of 10 cm. If the time constant $RC \gg 2\,\mathrm{ms}$, the signal amplitude is independent of $x_0$.

For many applications this is much too long. If one restricts oneself to the measurement of the electron component, which can be done by differentiating the signal, the total amplitude will not only be smaller, but also depend on the point in which the ionisation is produced, see Eq. (5.7).

This disadvantage can be overcome by mounting a grid between the anode and cathode (*Frisch grid* [5]). If the charged particle enters the larger volume between the grid and cathode, the produced charge carriers will first drift through this region which is shielded from the anode. Only when electrons penetrate through the grid, the signal on the working resistor $R$ will rise. Ions will not produce any signal on $R$ because their effect is screened by the grid. Consequently, this type of ionisation chamber with a Frisch grid measures only the electron signal which, in this configuration, is independent of the ionisation production region, as long as it is between the grid and the cathode.

Ionisation counters of this type are well suited for the detection of low-energy heavy particles. For example, 5 MeV $\alpha$ particles will deposit all their energy in a counter of 4 cm thickness filled with argon. Since

https://doi.org/10.1017/9781009401531.008 Published online by Cambridge University Press

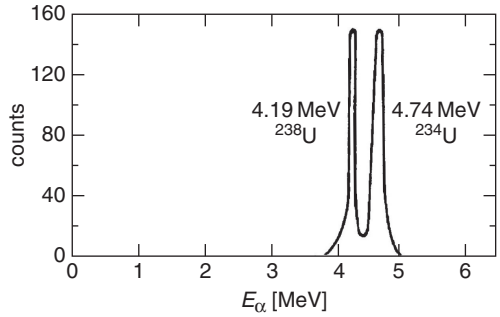


Fig. 5.2. Pulse-height spectrum of $\alpha$ particles emitted from a $^{234}U/^{238}U$ isotope mixture recorded with a Frisch grid ionisation chamber [4].

$W \approx 26\,\text{eV}$ for argon (see Table 1.2), the total number of electron–ion pairs will be

$$N = 5 \cdot 10^6\,\text{eV}/26\,\text{eV} = 1.9 \cdot 10^5\ . \tag{5.13}$$

Assuming a capacity of $C = 10\,\text{pF}$ we obtain the amplitude of the signal due to electrons as $\Delta U \approx 3\,\text{mV}$ which can be easily measured with rather simple electronics.

Figure 5.2 shows the pulse-height spectrum of $\alpha$ particles emitted from a mixture of radioisotopes $^{234}U$ and $^{238}U$ recorded by a Frisch grid ionisation chamber [4]. $^{234}U$ emits $\alpha$ particles with energies of 4.77 MeV (72%) and 4.72 MeV (28%), while $^{238}U$ emits mainly $\alpha$ particles of energy 4.19 MeV. Although the adjacent $\alpha$ energies of the $^{234}U$ isotope cannot be resolved, one can, however, clearly distinguish between the two different uranium isotopes.

Ionisation chambers can also be used in the spectroscopy of particles of higher charge because in this case the deposited energies are in general larger compared to those of singly charged minimum-ionising particles. And indeed, minimum-ionising particles passing the same 4 cm of argon deposit only about 11 keV which provides about 400 pairs. To detect such a small signal is a very difficult task!

Apart from planar ionisation counters, *cylindrical ionisation counters* are also in use. Because of the cylindrical arrangement of the electrodes, the electric field in this case is no longer constant but rather rises like $1/r$ to the anode wire (see, for example, the famous book [6]):

$$\vec{E} = \frac{\tau}{2\pi\varepsilon_0 r}\frac{\vec{r}}{r}\ , \tag{5.14}$$

https://doi.org/10.1017/9781009401531.008 Published online by Cambridge University Press

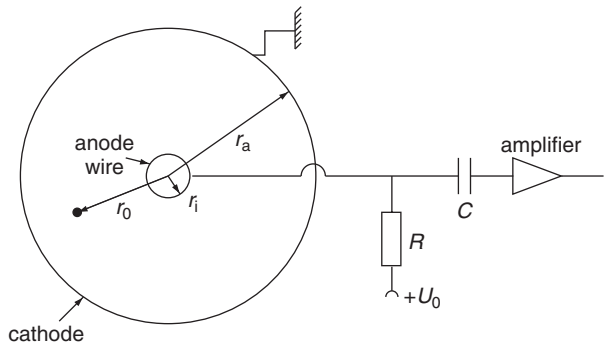


Fig. 5.3. Principle of operation of a cylindrical ionisation counter.

where $\tau$ is the linear charge density on the wire. The potential distribution is obtained by integration:

$$U = U(r_\mathrm{i}) - \int_{r_\mathrm{i}}^{r} E(r)\,\mathrm{d}r \ . \tag{5.15}$$

Here $r_\mathrm{a}$ – radius of cylindrical cathode, $r_\mathrm{i}$ – anode-wire radius (Fig. 5.3). By taking into account the boundary condition $U(r_\mathrm{i}) = U_0$, $U(r_\mathrm{a}) = 0$, Formulae (5.15), (5.14) provide $U(r)$ and $E(r)$ using the intermediate $C_\tau = 2\pi\varepsilon_0/\ln(r_\mathrm{a}/r_\mathrm{i})$ for the capacitance per unit length of the counter and $U_0 = \tau/C_\tau$:

$$U(r) = \frac{U_0 \ln(r/r_\mathrm{a})}{\ln(r_\mathrm{i}/r_\mathrm{a})} \ , \quad |\vec{E}(r)| = \frac{U_0}{r \ln(r_\mathrm{a}/r_\mathrm{i})} \ . \tag{5.16}$$

The field-dependent drift velocity can no longer assumed to be constant. The drift time of electrons is obtained by

$$T^- = \int_{r_0}^{r_\mathrm{i}} \frac{\mathrm{d}r}{v^-(r)} \ , \tag{5.17}$$

if the ionisation has been produced locally at a distance $r_0$ from the counter axis (e.g. by the absorption of an X-ray photon). The drift velocity can be expressed by the mobility $\mu(\vec{v}^- = \mu^- \cdot \vec{E})$, and in the approximation that the mobility does not depend on the field strength one obtains $(\vec{v} \| (-\vec{E}))$,

$$\begin{aligned} T^- &= -\int_{r_0}^{r_\mathrm{i}} \frac{\mathrm{d}r}{\mu^- \cdot E} = -\int_{r_0}^{r_\mathrm{i}} \frac{\mathrm{d}r}{\mu^- \cdot U_0} r \ln(r_\mathrm{a}/r_\mathrm{i}) \\ &= \frac{\ln(r_\mathrm{a}/r_\mathrm{i})}{2\mu^- \cdot U_0}(r_0^2 - r_\mathrm{i}^2) \ . \end{aligned} \tag{5.18}$$

https://doi.org/10.1017/9781009401531.008 Published online by Cambridge University Press

In practical cases the mobility does depend on the field strength, so that the drift velocity of electrons is not a linear function of the field strength. For this reason Eq. (5.18) presents only a rough approximation. The related signal pulse height can be computed in a way similar to Eq. (5.2) from

$$\frac{1}{2}CU^2 = \frac{1}{2}CU_0^2 - N\int_{r_0}^{r_\mathrm{i}} q \cdot \frac{U_0}{r\ln(r_\mathrm{a}/r_\mathrm{i})}\,\mathrm{d}r \tag{5.19}$$

to

$$\Delta U^- = -\frac{Ne}{C\ln(r_\mathrm{a}/r_\mathrm{i})}\ln(r_0/r_\mathrm{i}) \tag{5.20}$$

with $q = -e$ for drifting electrons and $C$ – the detector capacitance. It may clearly be seen that the signal pulse height in this case depends only logarithmically on the production point of ionisation.

The signal contribution due to the drift of the positive ions is obtained similarly,

$$\Delta U^+ = -\frac{Ne}{C}\frac{\ln(r_\mathrm{a}/r_0)}{\ln(r_\mathrm{a}/r_\mathrm{i})}\ . \tag{5.21}$$

The ratio of pulse heights originating from ions and electrons, respectively, is obtained as

$$\frac{\Delta U^+}{\Delta U^-} = \frac{\ln(r_\mathrm{a}/r_0)}{\ln(r_0/r_\mathrm{i})}\ . \tag{5.22}$$

Assuming that the ionisation is produced at a distance $r_\mathrm{a}/2$ from the anode wire, one gets

$$\frac{\Delta U^+}{\Delta U^-} = \frac{\ln 2}{\ln(r_\mathrm{a}/2r_\mathrm{i})}\ . \tag{5.23}$$

Since $r_\mathrm{a} \gg r_\mathrm{i}$, we obtain

$$\Delta U^+ \ll \Delta U^-\ , \tag{5.24}$$

i.e., for all practical cases (homogeneous illumination of the chamber assumed) the largest fraction of the signal in the cylindrical ionisation chamber originates from the movement of electrons. For typical values of $r_\mathrm{a} = 1\,\mathrm{cm}$ and $r_\mathrm{i} = 15\,\mu\mathrm{m}$ the signal ratio is

$$\Delta U^+/\Delta U^- = 0.12\ . \tag{5.25}$$

The pulse duration from ionisation chambers varies in a wide range depending on the gas mixtures (e.g., 80% Ar and 20% $CF_4$ provides very fast pulses, $\approx 35\,\mathrm{ns}$) [7]. The length of a tube ionisation chamber is almost unlimited, for example, a detector in the form of a gas dielectric cable with a length of 3500 m was used as a beam-loss monitor at SLAC [8].

https://doi.org/10.1017/9781009401531.008 Published online by Cambridge University Press

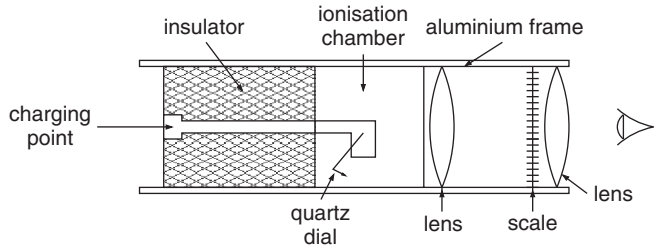


Fig. 5.4. Construction of an ionisation pocket dosimeter.

For radiation-protection purposes ionisation chambers are frequently used in a *current mode*, rather than a *pulse mode*, for monitoring the personal radiation dose. These *ionisation dosimeters* usually consist of a cylindrical air capacitor. The capacitor is charged to a voltage $U_0$. The charge carriers which are produced in the capacitor under the influence of radiation will drift to the electrodes and partially discharge the capacitor. The voltage reduction is a measure for the absorbed dose. The directly readable *pocket dosimeters* (Fig. 5.4) are equipped with an electrometer. The state of discharge can be read at any time using a built-in optics [9, 10].

### 5.1.2 Proportional counters

In ionisation chambers the primary ionisation produced by the incident particle is merely collected via the applied electric field. If, however, the field strength in some region of the counter volume is high, an electron can gain enough energy between two collisions to ionise another atom. Then the number of charge carriers increases. In cylindrical chambers the maximum field strength is around the thin-diameter anode wires due to the $1/r$ dependence of the electric field, see Eq. (5.16). The physics of electrical discharges in gases was developed by J.S. Townsend [11] and a good introduction is presented in [12, 13]. The signal amplitude is increased by the gas amplification factor $A$; therefore one gets, see Eq. (5.9),

$$\Delta U = -\frac{eN}{C} \cdot A \ . \tag{5.26}$$

The energy gain between two collisions is

$$\Delta E_{\mathrm{kin}} = eE \cdot \lambda_0 \ , \tag{5.27}$$

assuming that the field strength $\vec{E}$ does not change over the mean free path length $\lambda_0$. To consider the multiplication process let us take a simple model. When the electron energy $\Delta E_{\mathrm{kin}}$ at the collision is lower than a certain threshold, $I_{\mathrm{ion}}$, the electron loses its energy without ionisation,

https://doi.org/10.1017/9781009401531.008 Published online by Cambridge University Press

while, when $\Delta E_{\mathrm{kin}} > I_{\mathrm{ion}}$, ionisation nearly always occurs. The probability for an electron to pass the distance $\lambda > \lambda_{\mathrm{ion}} = I_{\mathrm{ion}}/(eE)$ without collision is $\mathrm{e}^{-\lambda_{\mathrm{ion}}/\lambda_0}$. Since an electron experiences $1/\lambda_0$ collisions per unit length, the total number of ionisation acts per unit length – or the *first Townsend coefficient* – can be written as

$$\alpha = \frac{1}{\lambda_0}\,\mathrm{e}^{-\lambda_{\mathrm{ion}}/\lambda_0}\ . \tag{5.28}$$

Taking into account the inverse proportionality of $\lambda_0$ to the gas pressure $p$, this can be rewritten as

$$\frac{\alpha}{p} = a \cdot \mathrm{e}^{\frac{b}{E/p}}\ , \tag{5.29}$$

where $a$ and $b$ are constants. In spite of its simplicity, this model reasonably describes the observed dependence when $a$ and $b$ are determined from experiment.

The first Townsend coefficient for different gases is shown in Fig. 5.5 for noble gases, and in Fig. 5.6 for argon with various additions of organic vapours. The first Townsend coefficient for argon-based gas mixtures at high electric fields can be taken from literature [14, 15].

If $N_0$ primary electrons are produced, the number of particles, $N(x)$, at the point $x$ is calculated from

$$\mathrm{d}N(x) = \alpha N(x)\,\mathrm{d}x \tag{5.30}$$

to be

$$N(x) = N_0\,\mathrm{e}^{\alpha x}\ . \tag{5.31}$$

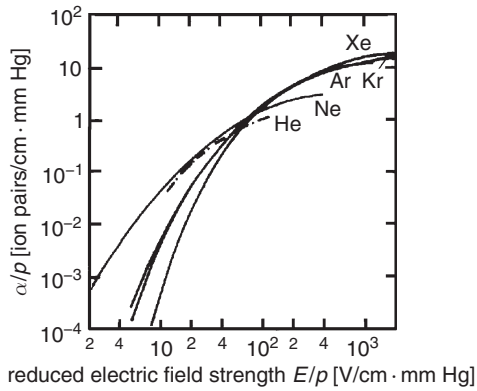


Fig. 5.5. First Townsend coefficient for some noble gases [15–18].

https://doi.org/10.1017/9781009401531.008 Published online by Cambridge University Press

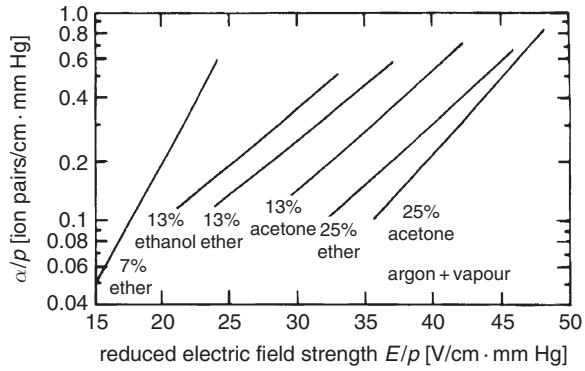


Fig. 5.6. First Townsend coefficient for argon with some organic vapour admixtures [16, 19, 20].

The first Townsend coefficient $\alpha$ depends on the field strength $\vec{E}$ and thereby on the position $x$ in the gas counter. Therefore, more generally, it holds that

$$N(x) = N_0 \cdot \mathrm{e}^{\int \alpha(x)\,\mathrm{d}x} \ , \tag{5.32}$$

where the gas amplification factor is given by

$$A = \exp\left\{\int_{r_\mathrm{k}}^{r_\mathrm{i}} \alpha(x)\,\mathrm{d}x\right\} \ . \tag{5.33}$$

The lower integration limit is fixed by the distance $r_\mathrm{k}$ from the centre of the gas counter, where the electric field strength exceeds the critical value $E_\mathrm{k}$ from which point on charge-carrier multiplication starts. The upper integration limit is the anode-wire radius $r_\mathrm{i}$.

The proportional range of a counter is characterised by the fact that the *gas amplification factor* $A$ takes a constant value. As a consequence, the measured signal is proportional to the produced ionisation. Gas amplification factors of up to $10^6$ are possible in the proportional mode. Typical gas amplifications are rather in the range between $10^4$ up to $10^5$.

If $U_\mathrm{th}$ is the threshold voltage for the onset of the proportional range, the gas amplification factor expressed by the detector parameters can be calculated to be [16]

$$A = \exp\left\{2\sqrt{\frac{kLCU_0 r_\mathrm{i}}{2\pi\varepsilon_0}}\left[\sqrt{\frac{U_0}{U_\mathrm{th}}} - 1\right]\right\} \ ; \tag{5.34}$$

where $U_0$ – applied anode voltage; $C = \frac{2\pi\varepsilon_0}{\ln r_\mathrm{a}/r_\mathrm{i}}$ – capacitance per unit length of the counter; $L$ – number of atoms/molecules per unit volume ($\frac{N_\mathrm{A}}{V_\mathrm{mol}} = 2.69 \cdot 10^{19}/\mathrm{cm}^3$) at normal pressure and temperature; $k$ is a

https://doi.org/10.1017/9781009401531.008 Published online by Cambridge University Press

gas-dependent constant on the order of magnitude $10^{-17}\,\mathrm{cm}^2/\mathrm{V}$, which can be obtained from the relation

$$\alpha = \frac{k \cdot L \cdot E_e}{e} \ , \tag{5.35}$$

where $E_e$ is the average electron energy (in eV) between two collisions [16]. In the case $U_0 \gg U_{\mathrm{th}}$ Eq. (5.34) simplifies to

$$A = \mathrm{const} \cdot \mathrm{e}^{U_0/U_{\mathrm{ref}}} \ , \tag{5.36}$$

where $U_{\mathrm{ref}}$ is a reference voltage.

Equation (5.36) shows that the gas amplification rises exponentially with the applied anode-wire voltage. The detailed calculation of the gas amplification is difficult [11, 21–30], However, it can be measured quite easily. Let $N_0$ be the number of primary charge carriers produced in the proportional counter which, for example, have been created by the absorption of an X-ray photon of energy $E_\gamma$ ($N_0 = E_\gamma/W$, where $W$ is the average energy that is required for the production of one electron–ion pair). The integration of the current at the output of the proportional counter leads to the gas-amplified charge

$$Q = \int i(t)\,\mathrm{d}t \ , \tag{5.37}$$

which is again given by the relation $Q = e \cdot N_0 \cdot A$. From the current integral and the known primary ionisation $N_0$ the gas amplification $A$ can be easily obtained.

At high field collisions of electrons with atoms or molecules can cause not only ionisation but also excitation. De-excitation is often followed by photon emission. The previous considerations are only true as long as photons produced in the course of the avalanche development are of no importance. These photons, however, will produce further electrons by the photoelectric effect in the gas or at the counter wall, which affect the avalanche development. Apart from gas-amplified primary electrons, secondary avalanches initiated by the photoelectric processes must also be taken into account. For the treatment of the gas amplification factor with inclusion of photons we will first derive the number of produced charge carriers in different generations.

In the first generation, $N_0$ primary electrons are produced by the ionising particle. These $N_0$ electrons are gas amplified by a factor $A$. If $\gamma$ is the probability that one photoelectron per electron is produced in the avalanche, an additional number of $\gamma(N_0 A)$ photoelectrons is produced via photoprocesses. These, however, are again gas amplified so that in the second generation $(\gamma N_0 A) \cdot A = \gamma N_0 A^2$ gas-amplified photoelectrons the

https://doi.org/10.1017/9781009401531.008 Published online by Cambridge University Press

anode wire, which again create $(\gamma N_0 A^2)\gamma$ further photoelectrons in the gas amplification process, which again are gas amplified themselves. The gas amplification $A_\gamma$ under inclusion of photons, therefore, is obtained from

$$\begin{aligned} N_0 A_\gamma &= N_0 A + N_0 A^2 \gamma + N_0 A^3 \gamma^2 + \cdots \\ &= N_0 A \cdot \sum_{k=0}^{\infty} (A\gamma)^k = \frac{N_0 A}{1 - \gamma A} \end{aligned} \tag{5.38}$$

to be

$$A_\gamma = \frac{A}{1 - \gamma A} \ . \tag{5.39}$$

The factor $\gamma$, which determines the gas amplification under inclusion of photons, is also called the *second Townsend coefficient*.

As the number of produced charges increases, they begin to have an effect on the external applied field and saturation effects occur. For $\gamma A \to 1$ the signal amplitude will be independent of the primary ionisation. The proportional or, rather, the saturated proportional region is limited by gas amplification factors around $A_\gamma = 10^8$.

The process of *avalanche formation* takes place in the immediate vicinity of the anode wire (Fig. 5.7). One has to realise that half of the total produced charge appears at the last step of the avalanche! The mean free paths of electrons are on the order of µm so that the total avalanche formation process according to Eq. (5.31) requires only about 10–20 µm. As a consequence, the effective production point of the charge (start of the avalanche process) is

$$r_0 = r_\mathrm{i} + k \cdot \lambda_0 \ , \tag{5.40}$$

where $k$ is the number of mean free paths which are required for the avalanche formation.

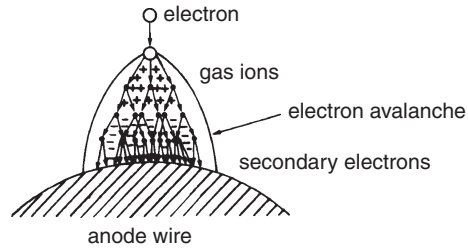


Fig. 5.7. Illustration of the avalanche formation on an anode wire in a proportional counter. By lateral diffusion a drop-shaped avalanche develops.

https://doi.org/10.1017/9781009401531.008 Published online by Cambridge University Press

The ratio of signal amplitudes which are caused by the drift of positive ions or electrons, respectively, is determined to be, see Eq. (5.22),

$$\frac{\Delta U^+}{\Delta U^-} = \frac{-\frac{Ne}{C}\frac{\ln(r_\mathrm{a}/r_0)}{\ln(r_\mathrm{a}/r_\mathrm{i})}}{-\frac{Ne}{C}\frac{\ln(r_0/r_\mathrm{i})}{\ln(r_\mathrm{a}/r_\mathrm{i})}} = \frac{\ln(r_\mathrm{a}/r_0)}{\ln(r_0/r_\mathrm{i})} = R \; . \tag{5.41}$$

The gas amplification factor cancels in this ratio because equal numbers of electrons and ions are produced.

With typical values of $r_\mathrm{a} = 1\,\mathrm{cm}$, $r_\mathrm{i} = 20\,\mu\mathrm{m}$ and $k\lambda = 10\,\mu\mathrm{m}$ this ratio is $R \approx 14$, which implies that in the proportional counter the signal on the anode wire is caused mainly by ions drifting slowly away from the wire and not by electrons which quickly drift in the direction of the wire.

The *rise time* of the electron signal can be calculated from Eq. (5.18). For electron mobilities in the range between $\mu^- = 100$ and $1000\,\mathrm{cm}^2/\mathrm{V\,s}$, an anode voltage of several hundred volts and typical detector dimensions as given above, the rise time is on the order of nanoseconds. The total ion drift time $T^+$ can be found analogously to Formula (5.18),

$$T^+ = \frac{\ln(r_\mathrm{a}/r_\mathrm{i})}{2\mu^+ \cdot U_0}(r_\mathrm{a}^2 - r_0^2) \; . \tag{5.42}$$

For the counter dimensions given above, $U_0 = 1000\,\mathrm{V}$ and an ion mobility at normal pressure equal to $\mu^+ = 1.5\,\mathrm{cm}^2/\mathrm{V\,s}$, the ion drift time $T^+$ is about 2 ms.

On the other hand, the time dependence of the signal induced by the motion of ions, $\Delta U^+(t)$, is quite non-linear. The voltage drop caused by the drift of the ions created near the anode wire ($r \approx r_\mathrm{i}$) to the point $r_1$ is, see Formula (5.21),

$$\Delta U^+(r_\mathrm{i}, r_1) = -\frac{Ne}{C}\frac{\ln(r_1/r_\mathrm{i})}{\ln(r_\mathrm{a}/r_\mathrm{i})} \; ; \tag{5.43}$$

and the ratio of this value to the total ion amplitude is

$$R = \frac{\Delta U^+(r_\mathrm{i}, r_1)}{\Delta U^+} = \frac{\ln(r_1/r_\mathrm{i})}{\ln(r_\mathrm{a}/r_\mathrm{i})} \; . \tag{5.44}$$

One can note that a large fraction of the signal is formed when ions move only a small part of the way from anode to cathode. As an example, let us calculate the $R$ value when the ion drifts from the anode ($r = r_\mathrm{i} = 20\,\mu\mathrm{m}$) to the distance $r_1 = 10\,r_\mathrm{i}$. Formula (5.44) gives $R \approx 0.4$ while the time that the ions require for this path is only $\Delta t^+(r_\mathrm{i}, 10\,r_\mathrm{i}) \approx 0.8\,\mu\mathrm{s}$. It means that by differentiating the signal with an $RC$ combination (as it is illustrated by Fig. 5.8) one can obtain a reasonably high and rather fast signal.

https://doi.org/10.1017/9781009401531.008 Published online by Cambridge University Press

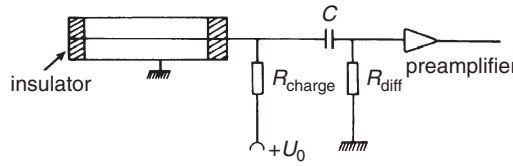


Fig. 5.8. Readout of a proportional counter.

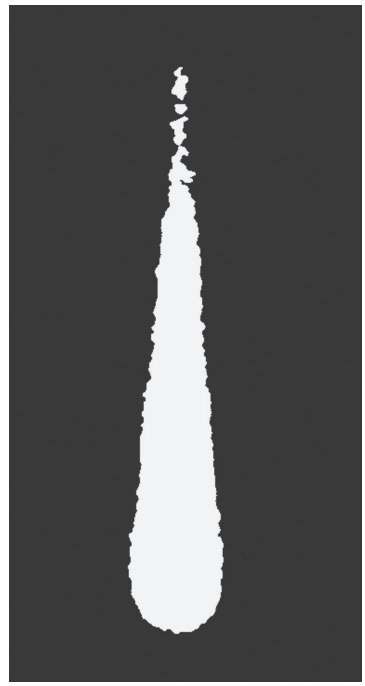

Fig. 5.9. Photographic reproduction of an electron avalanche [13, 16, 31, 32]. The photo shows the form of the avalanche. It was made visible in a cloud chamber (see Chap. 6) by droplets which had condensed on the positive ions.

Of course, if $R_{\text{diff}} \cdot C \approx 1\,\text{ns}$ is chosen, one can even resolve the time structure of the ionisation in the proportional counter.

Raether was the first to photograph *electron avalanches* (Fig. 5.9, [13, 16, 31, 32]). In this case, the avalanches were made visible in a cloud chamber by droplets which had condensed on the positive ions. The size of the luminous region of an avalanche in a proportional chamber is rather small compared to different gas-discharge operation modes, such as in Geiger–Müller or streamer tubes.

Proportional counters are particularly suited for the spectroscopy of X rays. Figure 5.10 shows the energy spectrum of 59.53 keV X-ray photons

https://doi.org/10.1017/9781009401531.008 Published online by Cambridge University Press

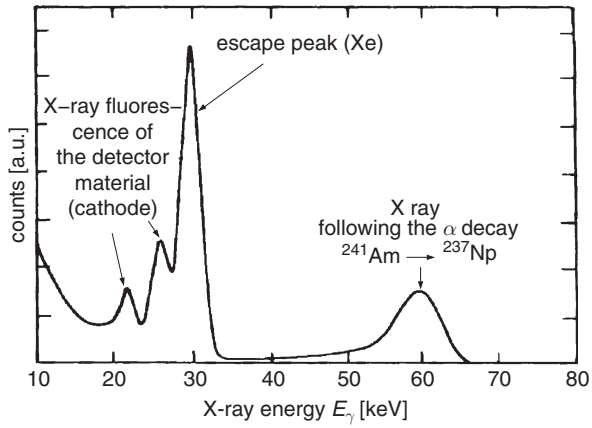


Fig. 5.10. Energy spectrum of 59.53 keV X-ray photons which are emitted in the $\alpha$ decay of $^{241}$Am, measured in a xenon proportional counter [33].

which are emitted in the $\alpha$ decay $^{241}_{95}\mathrm{Am} \rightarrow {}^{237}_{93}\mathrm{Np}^{*} + \alpha$ from the excited neptunium nucleus. The spectrum was measured in a xenon proportional counter. The characteristic X-ray lines of the detector material and the Xe *escape peak* are also seen [33]. The escape peak is the result of the following process. The incident X rays ionise the Xe gas in most cases in the K shell. The resulting photoelectron only gets the X-ray energy minus the binding energy in the K shell. If the gap in the K shell is filled up by electrons from outer shells, X rays characteristic of the gas may be emitted. If these characteristic X rays are also absorbed by the photoelectric effect in the gas, a total-absorption peak is observed; if the characteristic X rays leave the counter undetected, the escape peak is formed (see also Sect. 1.2.1).

Proportional counters can also be used for X-ray imaging. Special electrode geometries allow one- or two-dimensional readout with high resolution for X-ray synchrotron-radiation experiments which also work at high rates [34, 35]. The electronic imaging of ionising radiation with limited avalanches in gases has a wide field of application ranging from cosmic-ray and elementary particle physics to biology and medicine [36].

The energy resolution of proportional counters is limited by the fluctuations of the charge-carrier production and their multiplication. Avalanche formation is localised to the point of ionisation in the vicinity of the anode wire. It *does not* propagate along the anode wire.

### *5.1.3 Geiger counters*

The increase of the field strength in a proportional counter leads to a copious production of photons during the avalanche formation. As a

https://doi.org/10.1017/9781009401531.008 Published online by Cambridge University Press

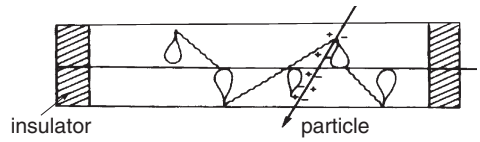


Fig. 5.11. Schematic representation of the transverse avalanche propagation along the anode wire in a Geiger counter.

consequence, the probability to produce further new electrons by the photoelectric effect increases. This photoelectric effect can also occur at points distant from the production of the primary avalanche. These electrons liberated by the photoelectric effect will initiate new avalanches whereby the discharge will propagate along the anode wire [37, 38] (Fig. 5.11).

The probability of photoelectron production per electron, $\gamma$, in the original avalanche becomes so large that the total number of charge carriers produced by various secondary and tertiary avalanches increases rapidly. As a consequence, the proportionality between the signal and the primary ionisation gets lost. The domain in which the liberated amount of charge does not depend on the primary ionisation is called the *Geiger mode*. The signal only depends on the applied voltage. In this mode of operation the signal amplitude corresponds to a charge signal of $10^8$ up to $10^{10}$ electrons per primary produced electron.

After the passage of a particle through a Geiger counter (also called *Geiger–Müller counter* [39]) a large number of charge carriers are formed all along the anode wire. The electrons are quickly drained by the anode, however, the ions form a kind of flux tube which is practically stationary. The positive ions migrate with low velocities to the cathode. Upon impact with the electrode they will liberate, with a certain probability, new electrons, thereby starting the discharge anew.

Therefore, the discharge must be interrupted. This can be achieved if the charging resistor $R$ is chosen to be so large that the momentary anode voltage $U_0 - IR$ is smaller than the threshold value for the Geiger mode (quenching by resistor).

Together with the total capacitance $C$ the time constant $RC$ has to be chosen in such a way that the voltage reduction persists until all positive ions have arrived at the cathode. This results in times on the order of magnitude of milliseconds, which strongly impairs the rate capability of the counter.

It is also possible to lower the applied external voltage to a level below the threshold for the Geiger mode for the ion drift time. This will, however, also cause long dead times. These can be reduced if the polarity of the electrodes is interchanged for a short time interval, thereby draining the

positive ions, which are all produced in the vicinity of the anode wire, to the anode which has been made negative for a very short period.

A more generally accepted method of quenching in Geiger counters is the method of *self-quenching*. In self-quenching counters a quench gas is admixed to the counting gas which is in most cases a noble gas. Hydrocarbons like methane ($CH_4$), ethane ($C_2H_6$), isobutane ($iC_4H_{10}$), alcohols like ethyl alcohol ($C_2H_5OH$) or methylal ($CH_2(OCH_3)_2$), or halides like ethyl bromide are suitable as quenchers. These additions will absorb photons in the ultraviolet range (wavelength 100–200 nm) thereby reducing their range to a few wire radii ($\approx 100\,\mu m$). The transverse propagation of the discharge proceeds only along and in the vicinity of the anode wire because of the short range of the photons. The photons have no chance to liberate electrons from the cathode by the photoelectric effect because they will be absorbed before they can reach the cathode.

After a flux tube of positive ions has been formed along the anode wire, the external field is reduced by this space charge by such an amount that the avalanche development comes to an end. The positive ions drifting in the direction of the cathode will collide on their way with quench-gas molecules, thereby becoming neutralised,

$$Ar^+ + CH_4 \rightarrow Ar + CH_4^+ \,. \tag{5.45}$$

The molecule ions, however, have insufficient energy to liberate electrons from the cathode upon impact. Consequently, the discharge stops by itself. The charging resistor, therefore, can be chosen to be smaller, with the result that time constants on the order of 1 μs are possible.

Contrary to the proportional mode, the discharge propagates along the whole anode wire in the Geiger mode. Therefore, it is impossible to record two charged particles in one Geiger tube at the same time. This is only achievable if the lateral propagation of the discharge along the anode wire can be interrupted. This can be accomplished by stretching insulating fibres perpendicular to the anode wire or by placing small droplets of insulating material on the anode wire. In these places the electric field is so strongly modified that the avalanche propagation is stopped. This locally *limited Geiger mode* allows the simultaneous registration of several particles on one anode wire. However, it has the disadvantage that the regions close to the fibres are inefficient for particle detection. The inefficient zone is typically 5 mm wide. The readout of simultaneous particle passages in the limited Geiger range is done via segmented cathodes.

### *5.1.4 Streamer tubes*

In Geiger counters the fraction of counting gas to quenching gas is typically 90:10. The anode wires have diameters of 30 μm and the anode

https://doi.org/10.1017/9781009401531.008 Published online by Cambridge University Press

voltage is around 1 kV. If the fraction of the quenching gas is considerably increased, the lateral propagation of the discharge along the anode wire can be completely suppressed. One again obtains, as in the proportional counter, a localised discharge with the advantage of large signals (gas amplification $\geq 10^{10}$ for sufficiently high anode voltages), which can be processed without any additional preamplifiers. These *streamer tubes* (Iarocci tubes, also developed by D.M. Khazins) [40–43] are operated with 'thick' anode wires between 50 μm and 100 μm diameter. Gas mixtures with $\leq$ 60% argon and $\geq$ 40% isobutane can be used. Streamer tubes operated with pure isobutane also proved to function well [44]. In this mode of operation the transition from the proportional range to streamer mode proceeds avoiding the Geiger discharges.

Figure 5.12 shows the amplitude spectra from a cylindrical counter with anode-wire diameter 100 μm, filled with argon/isobutane in proportion 60:40 under irradiation of electrons from a $^{90}$Sr source [45]. At relatively low voltages of 3.2 kV small proportional signals caused by electrons are seen. At higher voltages (3.4 kV) for the first time streamer signals

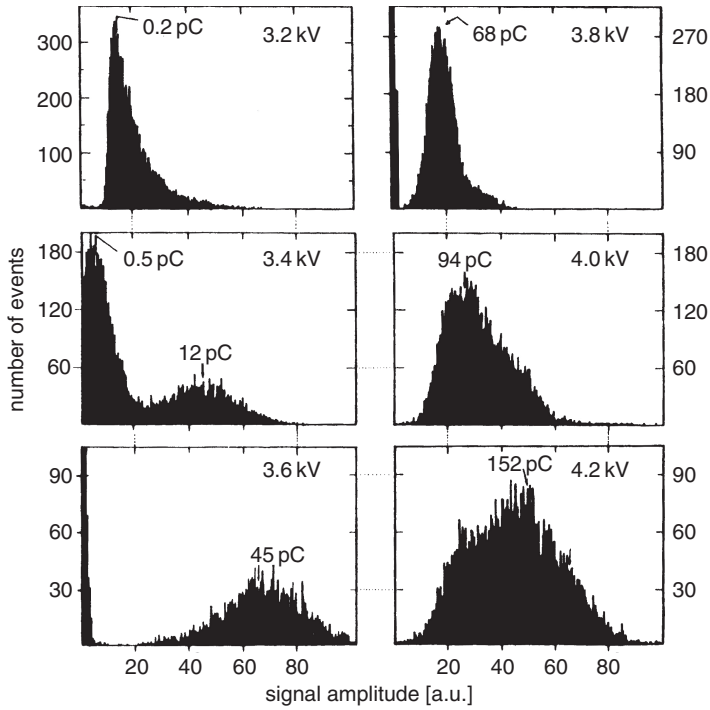


Fig. 5.12. Amplitude spectra of charge signals in a streamer tube. With increasing anode voltage the transition from the proportional to the streamer mode is clearly visible [45].

https://doi.org/10.1017/9781009401531.008 Published online by Cambridge University Press

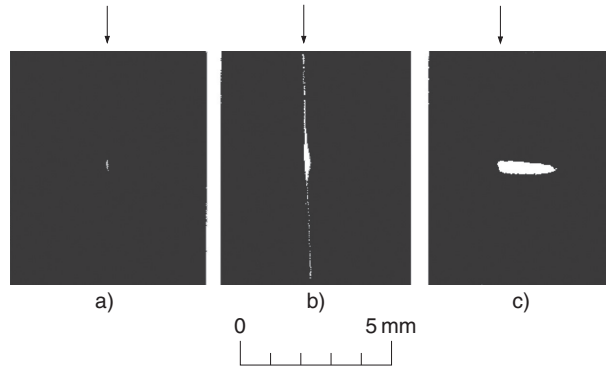


Fig. 5.13. Gas discharges in (a) a proportional counter, (b) a Geiger counter and (c) a self-quenching streamer tube; the arrows indicate the position of the anode wire [46].

with distinctly higher amplitudes also occur along with the proportional signals. For even higher voltages the proportional mode completely disappears, so that from 4 kV onwards only streamer signals are observed. The charge collected in the streamer mode does not depend on the primary ionisation.

The streamer mode develops from the proportional mode via the large number of produced photons which are re-absorbed in the immediate vicinity of the original avalanche via the photoelectric effect and are the starting point of new secondary and tertiary avalanches which merge with the original avalanche.

The photographs in Fig. 5.13 [46] demonstrate the characteristic differences of discharges in the proportional counter (a), Geiger counter (b) and a *self-quenching streamer tube* (c). In each case the arrows indicate the position of the anode wire.

Figure 5.14 presents the counting-rate dependence on the voltage for different proportion of filling gases. As has been discussed, streamer tubes have to be operated at high voltages ($\approx 5$ kV). They are, however, characterised by an extremely long efficiency plateau ($\approx 1$ kV) which enables a stable working point.

The onset of the efficiency, of course, depends on the threshold of the discriminator used. The upper end of the plateau is normally determined by after-discharges and noise. It is not recommended to operate streamer tubes in this region because electronic noise and *after-discharges* cause additional dead times, thereby reducing the rate capability of the counter.

If 'thick' anode wires are used, the avalanche is caused mostly by only one primary electron and the discharge is localised to the side of the anode wire which the electron approaches. The signals can be directly measured

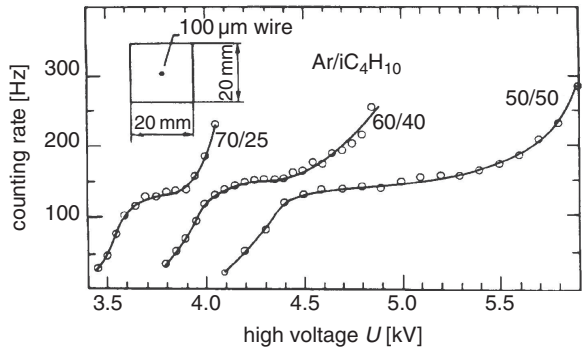


Fig. 5.14. Dependence of the counting rate on the high voltage in a streamer tube [45].

on the anode wire. Additionally or alternatively, one can also record the signals induced on the cathodes. A segmentation of the cathodes allows the determination of the track position along the anode wire.

Because of the simple mode of operation and the possibility of multi-particle registration on one anode wire, streamer tubes are an excellent candidate for sampling elements in calorimeters. A fixed charge signal $Q_0$ is recorded per particle passage. If a total charge $Q$ is measured in a streamer tube, the number of equivalent particles passing is calculated to be $N = Q/Q_0$.

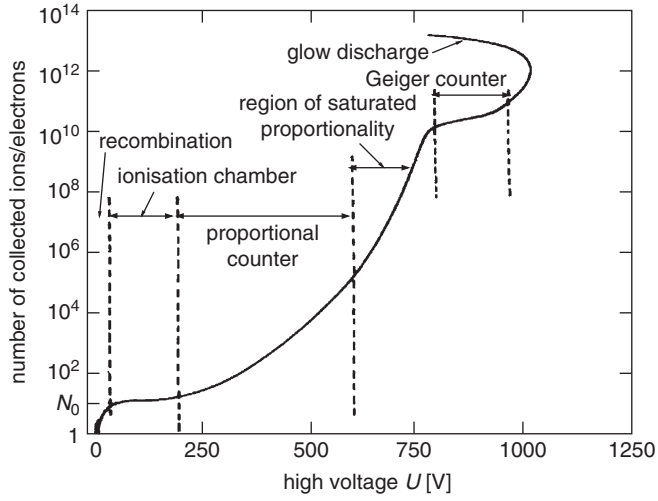


Fig. 5.15. Characterisation of the modes of operation of cylindrical gas detectors (after [16]). When the high voltage is increased beyond the Geiger regime (for counters with small-diameter anode wires), a *glow discharge* will develop and the voltage breaks down. This will normally destroy the counter.

https://doi.org/10.1017/9781009401531.008 Published online by Cambridge University Press

The choice of the high voltage, of the counting gas or anode-wire diameter, respectively, determines the discharge and thereby the operation mode of cylindrical counters. Figure 5.15 shows the different regions of operation in a comprehensive fashion (after [16]).

## 5.2 Ionisation detectors with liquids

Ionisation chambers filled with liquids have the advantage compared to gas-filled detectors of a density which is a factor of 1000 times higher. It implies a 1000-fold energy absorption in these media for a relativistic particle and the photon-detection efficiency increases by the same factor. Therefore, ionisation chambers filled with liquids are excellent candidates for sampling and homogeneous-type calorimeters [47–51].

The average energy for the production of an electron–ion pair in liquid argon (LAr) is 24 eV, and in liquid xenon (LXe) it is 16 eV. A technical disadvantage, however, is related to the fact that noble gases only become liquid at low temperatures. Typical temperatures of operation are 85 K for LAr, 117 K for LKr and 163 K for LXe. Liquid gases are homogeneous and therefore have excellent counting properties. Problems may, however, arise with electronegative impurities which must be kept at an extremely low level because of the slow drift velocities in the high-density liquid counting medium. To make operation possible, the absorption length $\lambda_{ab}$ of electrons must be comparable to the electrode distance. This necessitates that the concentration of electronegative gases such as $O_2$ be reduced to the level on the order of 1 ppm ($\equiv 10^{-6}$). The drift velocity in pure liquid noble gases at field strengths around 10 kV/cm, which are typical for *LAr counters*, is of the order 0.4 cm/μs. The addition of small amounts of hydrocarbons (e.g. 0.5% $CH_4$) can, however, increase the drift velocity significantly. This originates from the fact that the admixture of molecular gases changes the average electron energy. The electron scattering cross section, in particular, in the vicinity of the Ramsauer minimum [17, 52–56], is strongly dependent on the electron energy. So, small energy changes can have dramatic influence on the drift properties.

The ion mobility in liquids is extremely small. The induced charge due to the ion motion has a rise time so slow that it can hardly be used electronically.

The processes of charge collection and the output signal can be considered in the same way as for gaseous ionisation counters (Sect. 5.1.1). Often the integration time in the readout electronics is chosen much shorter than the electron drift time. This decreases the pulse height but makes the signal faster and reduces the dependence on the point of ionisation production.

https://doi.org/10.1017/9781009401531.008 Published online by Cambridge University Press

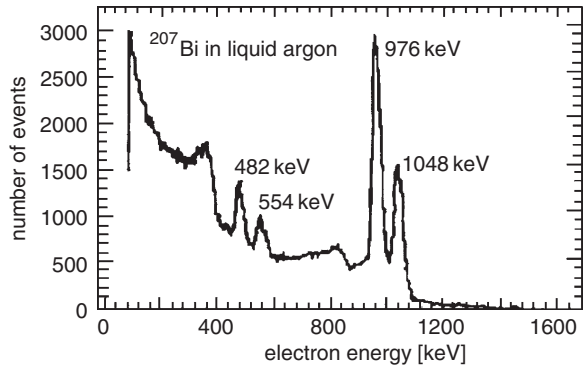


Fig. 5.16. Energy spectrum of conversion electrons from the isotope $^{207}$Bi in a liquid-argon chamber [57]. The spectrum also shows the Compton edges of the 570 keV and 1064 keV photons.

Figure 5.16 shows the energy spectrum of conversion electrons from $^{207}$Bi, recorded with a liquid-argon ionisation chamber. The $^{207}$Bi nuclei decay by electron capture into excited states of lead nuclei. De-excitation occurs by the emission of 570 keV and 1064 keV photons or by transfer of this excitation energy to the electrons at K and L shells of lead (see Table 3.3, Appendix 5). Thus, two K and L line pairs corresponding to the nuclear level transitions of 570 keV and 1064 keV are seen in the spectrum. The liquid-argon chamber separates the K and L electrons relatively well and achieves a resolution of $\sigma_E = 11\,\text{keV}$ [57].

The operation of *liquid-noble-gas ionisation chambers* requires cryogenic equipment. This technical disadvantage can be overcome by the use of *'warm' liquids*. The requirements for such 'warm' liquids, which are already in the liquid state at room temperature, are considerable: they must possess excellent drift properties and they must be extremely free of electronegative impurities ($< 1\,\text{ppb}$). The molecules of the 'warm' liquid must have a high symmetry (i.e. a near spherical symmetry) to allow favourable drift properties. Some organic substances like tetramethylsilane (TMS) or tetramethylpentane (TMP) are suitable as 'warm' liquids [49, 58–61].

Attempts to obtain higher densities, in particular, for the application of liquid ionisation counters in calorimeters, have also been successful. This can be achieved, for example, if the silicon atom in the TMS molecule is replaced by lead or tin (tetramethyltin (TMT) [62] or tetramethyllead). The flammability and toxicity problems associated with such materials can be handled in practice, if the liquids are sealed in vacuum-tight containers. These 'warm' liquids show excellent *radiation hardness*. Due to the high fraction of hydrogen they also allow for compensation of signal amplitudes for electrons and hadrons in calorimeters (see Chap. 8).

Obtaining gas amplification in liquids by increasing the working voltage has also been investigated, in a fashion similar to cylindrical ionisation chambers. This has been successfully demonstrated in small prototypes; however, it has not been reproduced on a larger scale with full-size detectors [63–65].

In closing, one should remark that *solid argon* can also be used successfully as a counting medium for ionisation chambers [66].

## 5.3 Solid-state ionisation counters

*Solid-state detectors* are essentially ionisation chambers with solids as a counting medium. Because of their high density compared to gaseous detectors, they can absorb particles of correspondingly higher energy. Charged particles or photons produce *electron–hole pairs* in a crystal. An electric field applied across the crystal allows the produced charge carriers to be collected.

The operating principle of solid-state detectors can be understood from the *band model of solids*. An introduction to the band theory of solids can be found, for example, in [67]. In the frame of this theory, the discrete electron energy levels of individual atoms or ions within a whole crystal are merged forming energy bands, as it is shown in Fig. 5.17. According to the Pauli exclusion principle, each band can contain only a finite number of electrons. So, some low energy bands are fully filled with electrons while the high energy bands are empty, at least at low temperature. The lowest partially filled or empty band is called *conduction band* while the highest fully filled band is referred to as *valence band*. The gap between the top of the valence band, $V_V$, and the bottom of the conduction band, $V_C$, is called *forbidden band* or *energy gap* with a width of $E_g = V_C - V_V$.

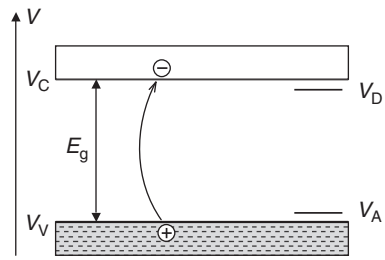


Fig. 5.17. Band structure of solid-state material. $V_V$ and $V_C$ are the top of valence band and bottom of the conduction band; $E_g$ – forbidden gap; $V_A$ and $V_D$ – acceptor and donor levels.

https://doi.org/10.1017/9781009401531.008 Published online by Cambridge University Press

When the 'conduction band' is partially filled, electrons can move easily under the influence of an electric field, hence, this solid is a conductor. Such a material cannot be used as an ionisation counter. The solids which have basically empty conduction bands are divided conventionally into insulators (specific resistivity $10^{14}$–$10^{22}\,\Omega\,\mathrm{cm}$ at room temperature) and semiconductors ($10^{9}$–$10^{-2}\,\Omega\,\mathrm{cm}$). The electric charge in these materials is carried by electrons which have been excited to the conduction band from the valence band. The corresponding vacancies in the valence band are called *holes* and are able to drift in the electric field as well. The main difference between insulators and semiconductors lies in the value of $E_\mathrm{g}$. For insulators it is typically $E > 3\,\mathrm{eV}$ while for semiconductors it is in the range of 1 eV.

Insulators are not widely used as ionisation counters. The main reasons are the low hole mobility in most of such crystals as well as the necessity of using very high-purity crystals. *Impurities* can create deep traps in wide-gap solids causing polarisation of the crystal under irradiation. The common solid-state ionisation counters are based on semiconductors.

The *specific resistivity* of the material is determined as

$$\varrho = \frac{1}{e(n\mu_e + p\mu_p)} \ , \tag{5.46}$$

where $n$ and $p$ are electron and hole concentrations, respectively, while $\mu_e$ and $\mu_p$ are their mobilities and $e$ is the elementary charge.

In a pure semiconductor the electron concentration, $n$, is equal to the hole concentration, $p$. These values can be approximated by the expression [68, 69]

$$n = p \approx 5 \cdot 10^{15}\,(T[\mathrm{K}])^{3/2}\,\mathrm{e}^{-E_\mathrm{g}/(2kT)} \ , \tag{5.47}$$

where $T$ is the temperature in K. For silicon with a band gap of $E_\mathrm{g} = 1.07\,\mathrm{eV}$ Eq. (5.47) results in $n \approx 2 \cdot 10^{10}\,\mathrm{cm}^{-3}$ at $T = 300\,\mathrm{K}$. Taking $\mu_e = 1300\,\mathrm{cm}^2\,\mathrm{s}^{-1}\,\mathrm{V}^{-1}$ and $\mu_p = 500\,\mathrm{cm}^2\,\mathrm{s}^{-1}\,\mathrm{V}^{-1}$ one gets an estimation for the specific resistivity, $\varrho \approx 10^5\,\Omega\,\mathrm{cm}$. For Ge ($E_\mathrm{g} = 0.7\,\mathrm{eV}$, $\mu_e = 4000\,\mathrm{cm}^2\,\mathrm{s}^{-1}\,\mathrm{V}^{-1}$, $\mu_p = 2000\,\mathrm{cm}^2\,\mathrm{s}^{-1}\,\mathrm{V}^{-1}$) the specific resistivity is about one order of magnitude lower. The impurities, even at low level, which almost always exist in the material, can substantially decrease these values.

Thus, semiconductors are characterised by a relatively high dark current. To suppress this, usually multilayer detectors containing layers with different properties are built. Electron and hole concentrations in these layers are intentionally changed by special doping.

Germanium and silicon have four electrons in the outer shell. If an atom with five electrons in the outer shell, like phosphorus or arsenic, is

incorporated to the crystal lattice, the fifth electron of the impurity atom is only weakly bound and forms a *donor level* $V_D$ that is just under but very close to the conduction band (see Fig. 5.17). Typically, the difference $V_C - V_D$ is in the range of 0.05 eV and this electron can easily be lifted to the conduction band. Material with an impurity of this type has a high concentration of free electrons and is therefore referred to as *n-type semiconductor*.

If trivalent electron acceptor impurities like boron or indium are added to the lattice, one of the silicon bonds remains incomplete. This *acceptor level*, which is about 0.05 eV above the edge of the valence band ($V_A$ in Fig. 5.17), tries to attract one electron from a neighbouring silicon atom creating a hole in the valence band. This type of material with high concentration of free holes is referred to as *p-type semiconductor*.

Let us consider the phenomena of a *pn* junction at the interface of two semiconductors of *p* and *n* type. The electrons of the *n*-type semiconductor diffuse into the *p* type, and the holes from the *p* type to the *n*-type region. This leads to the formation of a space-charge distribution shown in Fig. 5.18. The positive charge in the *n*-type region and the negative charge in *p*-type area provide the electric field which draws the free electrons and holes to the opposite direction out of the region of the electric field. Thus, this area has a low concentration of free carriers and is called the *depletion region* or *depletion layer*. When no external voltage is applied, the diffusion of carriers provides a contact potential, $U_c$, which is typically $\approx 0.5$ V.

The *pn junction* has the properties of a diode. At a 'direct' bias, when an external positive voltage is applied to the *p* region, the depletion area shortens causing a large direct current. At *reverse bias*, when an external positive voltage is applied to the *n* region, the depletion layer increases. A detailed consideration of the physics of *pn* junctions is given, for example, in [69] and its application to semiconductor detectors can be found in [68]. Electron–hole pairs released by photons interacting in the depletion area or by charged particles crossing the depletion layer are separated by the electric field and the carriers are collected by the electrodes inducing a current pulse. It is worth mentioning that electron–hole pairs created beyond the depletion layer do not produce an electric pulse since the electric field outside the *pn* junction is negligible due to the high charge-carrier concentration there.

Thus, a semiconductor device with a *pn* junction can be used as an ionisation detector. The total charge collected by this detector is proportional to the energy deposited in the depletion layer. Usually, one of the two semiconductor layers (*p* or *n*) has a much higher carrier concentration than the other. Then the depletion region extends practically all over the

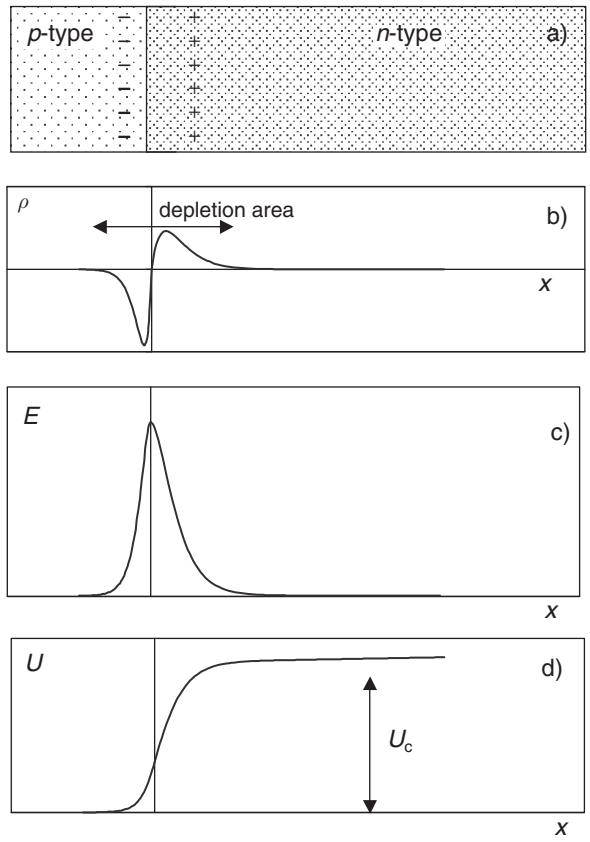


Fig. 5.18. (a) Working principle of a *pn* semiconductor counter; (b) space-charge distribution including all kinds of charge carriers: free electrons and holes, fixed positive non-compensating ions, electrons captured at acceptor levels; (c) electric field; (d) potential distribution. When no external voltage is applied, the maximum potential is equal to the contact voltage $U_c$.

area with low carrier concentration and, hence, high resistivity. The width of the depletion area, $d$, in this case can be expressed as [68]

$$d = \sqrt{2\varepsilon(U + U_c)\mu\varrho_d} \ , \tag{5.48}$$

where $U$ is the external *reverse-bias voltage*, $\varepsilon$ the dielectric constant of the material ($\varepsilon = 11.9\,\varepsilon_0 \approx 1\,\mathrm{pF/cm}$), $\varrho_d$ the specific resistivity of the low-doped semiconductor, and $\mu$ the mobility of the main carriers in the low-doped area. This expression leads to

$$d \approx 0.3\sqrt{U_n \cdot \varrho_p}\ \mu\mathrm{m} \tag{5.49}$$

https://doi.org/10.1017/9781009401531.008 Published online by Cambridge University Press

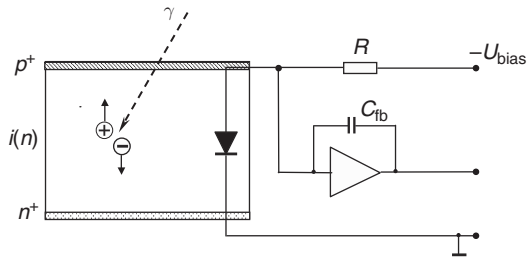


Fig. 5.19. Principle of construction of a *p–i–n* solid state detector along with its readout by a charge-sensitive preamplifier.

for *p*-doped silicon and

$$d \approx 0.5\sqrt{U_\mathrm{n} \cdot \varrho_\mathrm{n}}\ \mu\mathrm{m} \tag{5.50}$$

for *n*-doped silicon. $U_\mathrm{n}$ is the reverse-bias voltage (in volts, $= U/\mathrm{V}$), $\varrho_\mathrm{p,n}$ the specific resistivity in the *p*- or *n*-doped silicon in $\Omega\,\mathrm{cm}$ ($= \varrho_\mathrm{d}/\Omega\,\mathrm{cm}$). A typical value $\varrho_\mathrm{n} = 5 \cdot 10^3\,\Omega\,\mathrm{cm}$, at room temperature for *n*-type silicon used for detectors, gives a depletion-layer thickness of about $350\,\mu\mathrm{m}$ at $V = 100\,\mathrm{V}$.

The typical structure of a semiconductor detector is shown in Fig. 5.19 (the so-called *PIN diode structure*). An upper thin highly doped $p$ layer ($p^+$) is followed by a high-resistivity $i$ layer ($i$ is from *intrinsically conducting* or *insulator*, but actually the $i$ layer has a certain but very low $n$ or $p$ doping) and finally by a highly doped $n^+$ layer.*

In the example presented in Fig. 5.19 the *pn* junction appears at the $p^+$–$i(n)$ border and extends over the whole $i(n)$ area up to the $n^+$ layer that plays the rôle of an electrode. Usually, the upper $p^+$ layer is shielded by a very thin $SiO_2$ film.

Since *semiconductor diodes* do not have an intrinsic amplification, the output signal from this device is quite small. For example, a minimum-ionising particle crossing a depletion layer of $300\,\mu\mathrm{m}$ thickness produces about $3 \cdot 10^4$ electron–hole pairs corresponding to only $4.8 \cdot 10^{-15}\,\mathrm{C}$ of collected charge. Therefore, the processing of signals from solid-state detectors requires the use of low-noise *charge-sensitive amplifiers*, as shown in Fig. 5.19, followed by a shaper (see Chap. 14). To suppress electronics noise the integration time is usually relatively rather long – from hundreds of ns to tens of μs.

* Normally, only a very low concentration of dopant atoms is needed to modify the conduction properties of a semiconductor. If a comparatively small number of dopant atoms is added (concentration $\approx 10^{-8}$), the doping concentration is said to be low, or light, denoted by $n^-$ or $p^-$. If a much higher number is required ($\approx 10^{-4}$) then the doping is referred to as heavy, or high, denoted by $n^+$ or $p^+$.

https://doi.org/10.1017/9781009401531.008 Published online by Cambridge University Press

The charge collection time for such a detector can be estimated by taking an average field strength of $E = 10^3\,\mathrm{V/cm}$ and charge-carrier mobilities of $\mu = 10^3\,\mathrm{cm^2/V\,s}$:

$$t_\mathrm{s} = \frac{d}{\mu E} \approx 3 \cdot 10^{-8}\,\mathrm{s}\ . \tag{5.51}$$

The shape of the signal can be found in a similar way as for gaseous ionisation detectors (see Sect. 5.1.1), but for semiconductors the difference between mobilities of holes and electrons is only a factor of 2 to 3 in contrast to gases where ions are by 3 orders of magnitude less mobile than electrons. Therefore, the signal in semiconductor detectors is determined by both types of carriers and the collected charge does not depend on the point of where the ionisation was produced.

For $\alpha$ and electron spectroscopy the depletion layer in semiconductor counters should be very close to the surface to minimise the energy loss in an inactive material. The *surface-barrier detectors* meet this requirement. These detectors are made of an $n$-conducting silicon crystal by a special treatment of its surface producing a super-thin $p$-conducting film. A thin evaporated gold layer of several μm thickness serves as a high-voltage contact. This side is also used as an entrance window for charged particles.

Semiconductor counters with depletion areas up to 1 mm are widely used for $\alpha$-, low-energy $\beta$-, and X-ray detection and spectroscopy. Detectors of this type can be operated at room temperature as well as under cooling for dark-current suppression. In particle physics at high energies silicon detectors are typically used as high-resolution tracking devices in the form of strip, pixel or voxel counters (see Chaps. 7 and 13).

However, for gamma and electron spectroscopy in the MeV range as well as for $\alpha$ and proton energy measurements in the 10–100 MeV range the thickness of the depletion area should be much larger. To achieve this one should use a material with high intrinsic resistivity, as is seen from Formulae (5.48), (5.49), (5.50). One way of increasing the resistivity is cooling the device (see Formula (5.47)).

In the early 1960s high-resistivity-compensated silicon and germanium became available. In these materials the net free charge-carrier concentration was reduced by drifting lithium into $p$-conducting, e.g. boron-doped, silicon. Lithium has only one electron in the outer shell and is therefore an electron donor, since this outer electron is only weakly bound. Lithium atoms are allowed to diffuse into the $p$-conducting crystal at a temperature of about 400 ℃. Because of their small size, reasonable diffusion velocities are obtained with lithium atoms. A region is formed in which the number of boron ions is compensated by the lithium ions. This technology provides material with a specific resistivity of $3 \cdot 10^5\,\Omega\,\mathrm{cm}$ in the depletion layer, which is approximately equal to the intrinsic conductivity of silicon

https://doi.org/10.1017/9781009401531.008 Published online by Cambridge University Press

without any impurities. In this way, $p$–$i$–$n$ structures can be produced with relatively thin $p$ and $n$ regions and with $i$ zones up to 5 mm.

From the early 1980s on *high-purity germanium crystals* (HPGe) with impurity concentrations as low as $10^{10}\,\mathrm{cm}^{-3}$ became available. Nowadays, HPGe detectors have almost replaced the Ge(Li) type. HPGe detectors have the additional advantage that they only have to be cooled during operation, while Ge(Li) detectors must be permanently cooled to prevent the lithium ions from diffusing out of the intrinsically conducting region. At present HPGe detectors with an area up to $50\,\mathrm{cm}^2$ and a thickness of the sensitive layer up to 5 cm are commercially available, the largest coaxial-type HPGe detector has a diameter and a length of about 10 cm [70]. Usually, all Ge detectors operate at liquid-nitrogen temperatures, i.e. at $\approx 77\,\mathrm{K}$.

The energy resolution of semiconductor detectors can be approximated by the combination of three terms:

$$\sigma_E = \sqrt{\sigma_{\mathrm{eh}}^2 + \sigma_{\mathrm{noise}}^2 + \sigma_{\mathrm{col}}^2}\ , \tag{5.52}$$

where $\sigma_{\mathrm{eh}}$ is the statistical fluctuation of the number of electron–hole pairs, $\sigma_{\mathrm{noise}}$ the contribution of electronics noise, and $\sigma_{\mathrm{col}}$ the contribution of the non-uniformity of the charge collection efficiency and other technical effects.

For solid-state counters, just as with gaseous detectors, the statistical fluctuation of the number of produced charge carriers is smaller than Poissonian fluctuations, $\sigma_{\mathrm{P}} = \sqrt{n}$. The shape of a monoenergetic peak is somewhat asymmetric and narrower than a Gaussian distribution. The Fano factor $F$ (measurements for silicon and germanium give values from 0.08 to 0.16 [68], see also Chap. 1) modifies the Gaussian variance $\sigma_{\mathrm{P}}^2$ to $\sigma^2 = F\sigma_{\mathrm{P}}^2$, so that the electron–hole-pair statistics contribution to the energy resolution – because $E$ is proportional to $n$ – can be represented by

$$\frac{\sigma_{\mathrm{eh}}(E)}{E} = \frac{\sqrt{F\sigma_{\mathrm{P}}^2}}{n} = \frac{\sqrt{n}\sqrt{F}}{n} = \frac{\sqrt{F}}{\sqrt{n}}\ . \tag{5.53}$$

Since the number of electron–hole pairs is $n = E/W$, where $W$ is the average energy required for the production of one charge-carrier pair, one obtains

$$\frac{\sigma(E)}{E} = \frac{\sqrt{F \cdot W}}{\sqrt{E}}\ . \tag{5.54}$$

The properties of commonly used semiconductors are presented in Table 5.1.

Figure 5.20 presents the energy spectrum of photons from a $^{60}$Co radioactive source, as measured with a HPGe detector (Canberra GC

https://doi.org/10.1017/9781009401531.008 Published online by Cambridge University Press

Table 5.1. *Properties of commonly used semiconductors [68, 71]*

| Characteristic property | Si | Ge |
|---|---|---|
| Atomic number | 14 | 32 |
| Atomic weight | 28.09 | 72.60 |
| Density in g/cm$^3$ | 2.33 | 5.32 |
| Dielectric constant | 12 | 16 |
| Energy gap at 300 K in eV | 1.12 | 0.67 |
| Energy gap at 0 K in eV | 1.17 | 0.75 |
| Charge carrier density at 300 K in cm$^{-3}$ | $1.5 \cdot 10^{10}$ | $2.4 \cdot 10^{13}$ |
| Resistivity at 300 K in $\Omega$ cm | $2.3 \cdot 10^5$ | 47 |
| Electron mobility at 300 K in cm$^2$/V s | 1350 | 3900 |
| Electron mobility at 77 K in cm$^2$/V s | $2.1 \cdot 10^4$ | $3.6 \cdot 10^4$ |
| Hole mobility at 300 K in cm$^2$/V s | 480 | 1900 |
| Hole mobility at 77 K in cm$^2$/V s | $1.1 \cdot 10^4$ | $4.2 \cdot 10^4$ |
| Energy per e–h pair at 300 K in eV | 3.62 | $\approx 3$ for HPGe[a] |
| Energy per e–h pair at 77 K in eV | 3.76 | 2.96 |
| Fano factor[b] at 77 K | $\approx 0.15$ | $\approx 0.12$ |

[a] For room-temperature operation High Purity Germanium (HPGe) is required.
[b] The value of the Fano factor shows a large scatter in different publications, see [68].

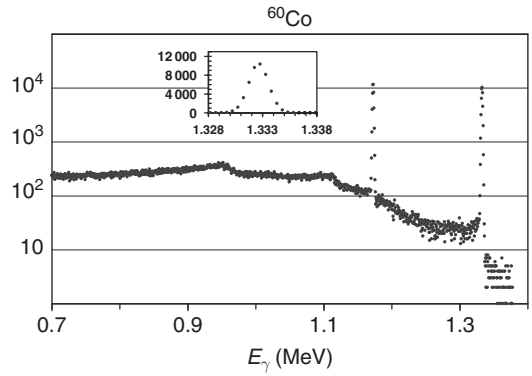


Fig. 5.20. Gamma spectrum from a $^{60}$Co source measured by a HPGe detector (by courtesy of V. Zhilich). The peaks correspond to the 1.17 MeV and 1.33 MeV $^{60}$Co $\gamma$ lines, while the two shoulders in the central part of the spectrum are caused by Compton edges related to the full-absorption lines (see Table 3.3 and Appendix 5).

https://doi.org/10.1017/9781009401531.008 Published online by Cambridge University Press

2518) [72]. The two $^{60}$Co $\gamma$ lines, 1.17 MeV and 1.33 MeV, are clearly seen, and the energy resolution at $E_\gamma = 1.33\,\text{MeV}$ is about 2 keV (FWHM) or $\text{FWHM}/E_\gamma \approx 1.5 \cdot 10^{-3}$. The theoretical limitation imposed by electron–hole-pair statistics on the energy resolution for this case can be estimated from Formula (5.54). Values of $W \approx 3\,\text{eV}$ and $F \approx 0.1$ lead to

$$\sigma(E)/E \approx 4.7 \cdot 10^{-4}\ ,\ \ \text{FWHM}/E = 2.35 \cdot \sigma(E)/E \approx 1.1 \cdot 10^{-3} \quad (5.55)$$

for $E_\gamma = 1.33\,\text{MeV}$. This result is not very far from the experimentally obtained detector parameters.

Although only silicon and germanium semiconductor detectors are discussed here, other materials like gallium arsenide (GaAs) [73, 74], cadmium telluride (CdTe) and cadmium–zinc telluride [75] can be used for particle detectors in the field of nuclear and elementary particle physics.

To compare the spectroscopic properties of solid-state detectors with other counters (see Sects. 5.1, 5.2, and 5.4), we have to note that the average energy required for the creation of an electron–hole pair is only $W \approx 3\,\text{eV}$. This parameter, according to Formulae (5.53) and (5.54), provides in principle the limitation for the energy resolution. For gases and liquid noble gases $W$ is approximately 10 times larger, $W \approx 20$–$30\,\text{eV}$, while for scintillation counters the energy required to produce one photoelectron at the photosensor is in the range of 50–100 eV. In addition, one cannot gain anything here from the Fano factor ($F \approx 1$).

Semiconductor counters are characterised by quantum transitions in the range of several electron volts. The energy resolution could be further improved if the energy absorption were done in even finer steps, such as by the break-up of Cooper pairs in *superconductors*. Figure 5.21 shows the amplitude distribution of current pulses, caused by manganese $K_\alpha$ and $K_\beta$ X-ray photons in an $Sn/SO_x/Sn$ tunnel-junction layer at $T = 400\,\text{mK}$. The obtainable resolutions are, in this case, already significantly better than the results of the best Si(Li) semiconductor counters [76].

For even lower temperatures ($T = 80\,\text{mK}$) resolutions of 17 eV FWHM for the manganese $K_\alpha$ line have been obtained with a *bolometer* made from a HgCdTe absorber in conjunction with a Si/Al calorimeter (Fig. 5.22) [77, 78].

With a bolometer, a deposited energy of 5.9 keV from $K_\alpha$ X rays is registered by means of a temperature rise. These microcalorimeters must have an extremely low heat capacity, and they have to be operated at cryogenic temperatures. In most cases they consist of an absorber with a relatively large surface (some millimetres in diameter), which is coupled to a semiconductor thermistor. The deposited energy is collected in the absorber part, which forms, together with the thermistor readout, a totally absorbing calorimeter. Such two-component bolometers allow one to obtain

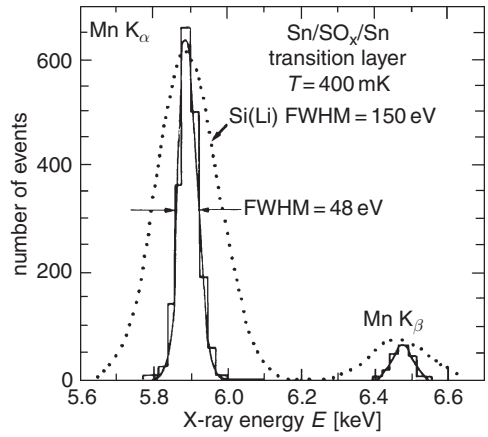


Fig. 5.21. Amplitude distribution of Mn $K_\alpha$ and Mn $K_\beta$ X-ray photons in an $Sn/SO_x/Sn$ tunnel-junction layer. The dotted line shows the best obtainable resolution with a Si(Li) semiconductor detector for comparison [76].

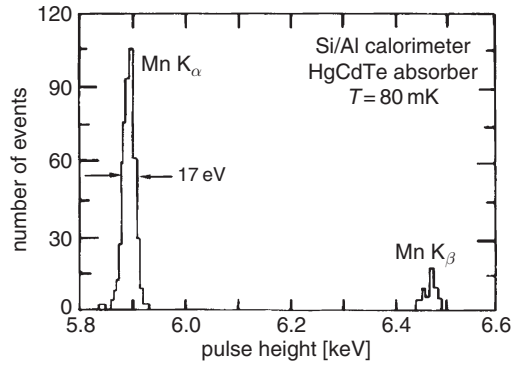


Fig. 5.22. Amplitude distribution of 5.9 keV and 6.47 keV X rays from the Mn $K_\alpha$ and $K_\beta$ lines in a bolometer consisting of a HgCdTe absorber and a Si/Al calorimeter. The $K_\alpha$ line corresponds to a transition from the L into the K shell, the $K_\beta$ line to a transition from the M into the K shell [78].

excellent energy resolution, but they cannot, at the moment, process high rates of particles since the decay time of the thermal signals is on the order of 20 μs. Compared to standard calorimetric techniques, which are based on the production and collection of ionisation electrons, bolometers have the large advantage that they can in principle also detect weakly or non-ionising particles such as slow magnetic monopoles, weakly interacting massive particles (WIMPs), astrophysical neutrinos, or, for example, primordial neutrino radiation as remnant from the Big Bang with energies

https://doi.org/10.1017/9781009401531.008 Published online by Cambridge University Press

around 0.2 meV ($\approx$ 1.9 K), corresponding to the 2.7 K microwave background radiation. The detection of these cosmological neutrinos is a real challenge for detector builders. Excellent energy resolution for X rays also has been obtained with large-area superconducting Nb/Al–$AlO_x$/Al/Nb *tunnel junctions* [79].

## 5.4 Scintillation counters

A *scintillator* is one of the oldest particle detectors for nuclear radiation. In the early times charged particles had been detected by light flashes emitted when the particles impinged on a zinc-sulphate screen. This light was registered with the naked eye. It has been reported that the sensitivity of the human eye can be significantly increased by a cup of strong coffee possibly with a small dose of strychnine.

After a longer period of accommodation in complete darkness, the human eye is typically capable of recognising approximately 15 photons as a light flash, if they are emitted within one tenth of a second and if their wavelength is matched to the maximum sensitivity of the eye.

The time span of a tenth of a second corresponds roughly to the time constant of the visual perception [80]. Chadwick [81] refers occasionally to a paper by Henri and Bancels [82, 83], where it is mentioned that an energy deposit of approximately 3 eV, corresponding to a single photon in the green spectral range, should be recognisable by the human eye [84].

New possibilities were opened in 1948, when it was found that crystals of *sodium iodide* are good scintillators and can be grown up to a large size [85]. These crystals in combination with photomultipliers were successfully exploited for gamma-ray spectroscopy [86].

The measurement principle of scintillation counters has remained essentially unchanged. The function of a scintillator is twofold: first, it should convert the excitation of, e.g., the crystal lattice caused by the energy loss of a particle into visible light; and, second, it should transfer this light either directly or via a light guide to an optical receiver (photomultiplier, photodiode, etc.) [87–89]. Reference [87] gives a detailed review of physical principles and characteristics of scintillation detectors.

The disadvantage of such indirect detection is that a much larger energy is required for the generation of one photoelectron than it is necessary for the creation of one electron–hole pair in solid-state ionisation detectors. We have to compare an amount of about 50 eV for the best scintillation counters with 3.65 eV for silicon detectors. But this drawback is compensated by the possibility to build a detector of large size and mass, up to tens of metres and hundreds of tons at relatively low cost of the scintillation material.

The main scintillator characteristics are: scintillation efficiency, light output, emission spectrum and decay time of the scintillation light. The *scintillation efficiency* $\varepsilon_{sc}$ is defined as the ratio of the energy of the emitted photons to the total energy absorbed in the scintillator. The *light output* $L_{ph}$ is measured as the number of photons per 1 MeV of energy absorbed in the scintillator. The *emission spectrum* usually has a maximum (sometimes more than one) at a characteristic wavelength $\lambda_{em}$. For light collection the index of refraction $n(\lambda)$ and the light attenuation length $\lambda_{sc}$ are important. The scintillation flash is characterised by a fast rise followed by a much longer exponential decay with a *decay time* $\tau_D$ characteristic of the scintillation material. Often, more than one exponential component is required to describe the light pulse shape. In that case several decay times $\tau_{D,i}$ are needed to describe the trailing edge of the pulse.

Scintillator materials can be inorganic crystals, organic compounds, liquids and gases. The scintillation mechanism in these scintillator materials is fundamentally different.

*Inorganic scintillators* are mostly crystals, pure ($Bi_4Ge_3O_{12}$, $BaF_2$, CsI, etc.) or doped with small amounts of other materials (NaI(Tl), CsI(Tl), LiI(Eu), etc.) [90, 91].

The *scintillation mechanism* in inorganic substances can be understood by considering the energy bands in crystals. Since the scintillator must be transparent for the emitted light, the number of free electrons in the conduction band should be small and the gap between valence and conduction bands should be wide enough, at least several eV. Halide crystals, which are most commonly used, are insulators. The valence band is completely occupied, but the conduction band is normally empty (Fig. 5.23). The energy difference between both bands amounts to about 3 eV to 10 eV.

Electrons are transferred from the valence band to the conduction band by the energy deposited by an incident charged particle or $\gamma$ ray. In the conduction band they can move freely through the crystal lattice. In this excitation process a hole remains in the valence band. The electron can

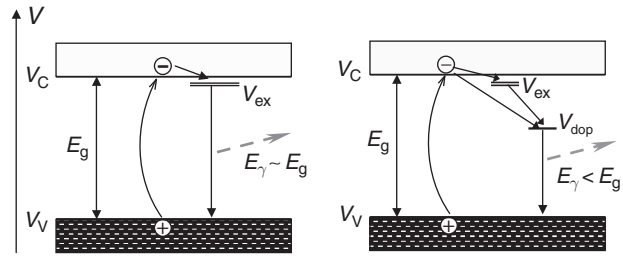


Fig. 5.23. Energy bands in a pure (left) and doped (right) crystal.

https://doi.org/10.1017/9781009401531.008 Published online by Cambridge University Press

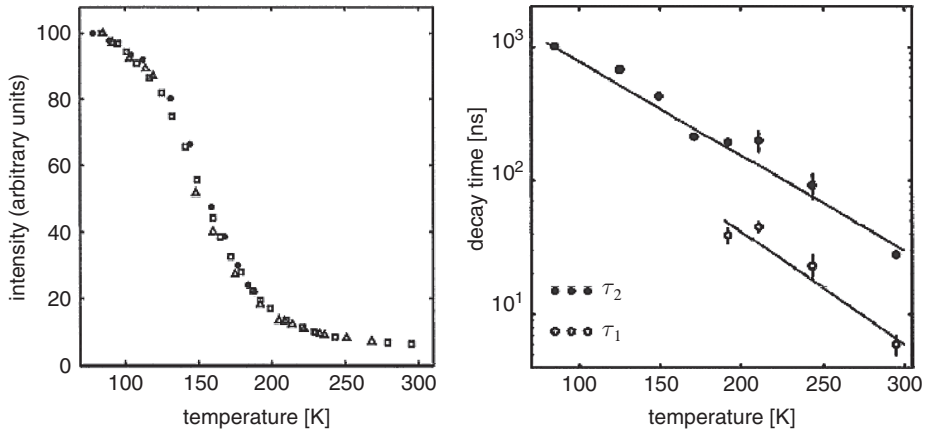


Fig. 5.24. Light output (left) and decay time (right) for a pure CsI crystal [92]. Two curves in the right-hand figure correspond to two decay-time constants.

recombine with the hole or create a bound state with a hole called exciton. The *exciton level* $V_{ex}$ is slightly below the lower edge of the conduction band, $V_C$. The exciton migrates in the crystal for some time and then can be de-excited in a collision with a phonon or it just recombines emitting a photon corresponding to its excitation energy $E_{ex}$. At room temperature the probability of photon emission is low while at cryogenic temperatures this mechanism mainly defines the exciton lifetime. So, the scintillation efficiency becomes quite high for pure alkali–halide crystals at low temperatures. Figure 5.24 shows the temperature dependence of the light output and the decay time of pure CsI [92]. It can be seen from the figure that the light output increases at low temperature while the decay time of the light flash becomes longer.

To improve the scintillation efficiency at room temperature, dopant impurities, which act as *activator centres*, are deliberately introduced into the crystal lattice. These impurities are energetically localised between the valence and the conduction band thereby creating additional energy levels $V_{dop}$. Excitons or free electrons can hit an activator centre whereby their binding energy may be transferred (see Fig. 5.23). The excitation energy of the activator centre is handed over to the crystal lattice in form of lattice vibrations (phonons) or it is emitted as light. A certain fraction of the energy deposited in the crystal is thereby emitted as luminescence radiation. This radiation can be converted to a voltage signal by a photosensitive detector. The decay time of the scintillator depends on the lifetimes of the excited levels.

Table 5.2 shows the characteristic parameters of some inorganic scintillators [93–98]. As it can be seen from the table, inorganic scintillators

https://doi.org/10.1017/9781009401531.008 Published online by Cambridge University Press

Table 5.2. *Characteristic parameters of some inorganic scintillators [93–98]*

| Scintillator | Density $\varrho$ [g/cm$^3$] | $X_0$ [cm] | $\tau_D$ [ns] | $L_{ph}$, $N_{ph}$ [per MeV] | $\lambda_{em}$ [nm] | $n(\lambda_{em})$ |
|---|---|---|---|---|---|---|
| NaI(Tl) | 3.67 | 2.59 | 230 | $3.8 \cdot 10^4$ | 415 | 1.85 |
| LiI(Eu) | 4.08 | 2.2 | 1400 | $1 \cdot 10^4$ | 470 | 1.96 |
| CsI | 4.51 | 1.85 | 30 | $2 \cdot 10^3$ | 315 | 1.95 |
| CsI(Tl) | 4.51 | 1.85 | 1000 | $5.5 \cdot 10^4$ | 550 | 1.79 |
| CsI(Na) | 4.51 | 1.85 | 630 | $4 \cdot 10^4$ | 420 | 1.84 |
| $Bi_4Ge_3O_{12}$ (BGO) | 7.13 | 1.12 | 300 | $8 \cdot 10^3$ | 480 | 2.15 |
| $BaF_2$ | 4.88 | 2.1 | 0.7 | $2.5 \cdot 10^3$ | 220 | 1.54 |
| | | | 630 | $6.5 \cdot 10^3$ | 310 | 1.50 |
| $CdWO_4$ | 7.9 | 1.06 | 5000 | $1.2 \cdot 10^4$ | 540 | 2.35 |
| | | | 20 000 | | 490 | |
| $PbWO_4$ (PWO) | 8.28 | 0.85 | 10/30 | 70–200 | 430 | 2.20 |
| $Lu_2SiO_5$(Ce) (LSO) | 7.41 | 1.2 | 12/40 | $2.6 \cdot 10^4$ | 420 | 1.82 |

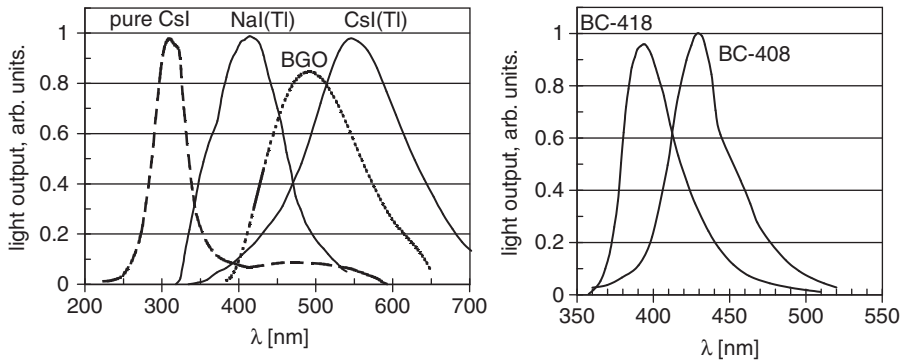


Fig. 5.25. The luminescence spectra of some scintillation crystals and plastic scintillators [94, 98]. The curves are arbitrarily scaled.

have decay times and light outputs in a wide range. Some of the scintillators are widely used in high energy physics experiments as well as in nuclear spectroscopy while others are still under study [91, 99].

The *luminescence spectra* of some inorganic scintillation crystals are shown in Fig. 5.25 in comparison to plastic-scintillator spectra, which are usually more narrow.

https://doi.org/10.1017/9781009401531.008 Published online by Cambridge University Press

Table 5.3. *Characteristic parameters of some organic scintillators [87, 93, 94, 102, 103]*

| Scintillator | base | density $\varrho$ [g/cm$^3$] | $\tau_D$ [ns] | $L_{ph}$, $N_{ph}$ [per MeV] | $\lambda_{em}$ [nm] | $n(\lambda_{em})$ |
|---|---|---|---|---|---|---|
| Anthracene | | 1.25 | 30 | 16 000 | 440 | 1.62 |
| BC-408 (BICRON) | PVT | 1.032 | 2.1 | 10 000 | 425 | 1.58 |
| BC-418 (BICRON) | PVT | 1.032 | 1.5 | 11 000 | 391 | 1.58 |
| UPS-89 (AMCRYS-H) | PS | 1.06 | 2.4 | 10 000 | 418 | 1.60 |
| UPS-91F (AMCRYS-H) | PS | 1.06 | 0.6 | 6 500 | 390 | 1.60 |

*Organic scintillators* are polymerised plastics, liquids or sometimes also crystals, although the latter are rarely used at present. Plastic scintillation materials most widely used now are usually based on polymers having benzene rings in their molecular structure. Such materials luminesce after charged-particle energy deposition. However, the emitted light is in the ultraviolet range and the absorption length of this light is quite short: the fluorescent agent is opaque for its own light. To obtain light output in the maximum-sensitivity wavelength range of the photomultiplier (typically 400 nm) one or two (sometimes even three) fluorescent agents are added to the basic material acting as *wavelength shifters*. For these compounds the excitation of the molecules of the basic polymer is transferred to the first fluorescent agent via the non-radiative Förster mechanism [100] and de-excitation of this fluorescent component provides light of a longer wavelength. If this wavelength is not fully adjusted to the sensitivity of the photocathode, the extraction of the light is performed by adding a second fluorescent agent to the scintillator, which absorbs the already shifted fluorescent light and re-emits it at lower frequency isotropically ('wavelength shifter'). The emission spectrum of the final component is then normally matched to the spectral sensitivity of the light receiver [101].

Table 5.3 lists the properties of some popular *plastic scintillator materials* in comparison with the organic crystal anthracene. The best plastic scintillators are based on polyvinyltoluene (PVT, polymethylstyrene) and polystyrene (PS, polyvinylbenzene). Sometimes a non-scintillating base, like PMMA (polymethyl methacrylate, 'Plexiglas' or 'Perspex'), is used with an admixture ($\approx 10\%$) of naphthalene. This scintillator is cheaper than the PVT- or PS-based ones and has a good transparency for its own light, but the light output is typically a factor of two lower than that of the best materials. Organic scintillators are characterised by short decay times, which lie typically in the nanosecond range.

The active components in an organic scintillator are either dissolved in an organic liquid or are mixed with an organic material to form a

polymerising structure. In this way liquid or plastic scintillators can be produced in almost any geometry. In most cases scintillator sheets of 1 mm up to 30 mm thickness are made.

All solid and liquid scintillators are characterised by a non-linear response to the energy deposition at very high ionisation density [87, 104, 105]. For example, the scintillation signal from a CsI(Tl) crystal normalised to the deposited energy is about a factor of two lower for a 5 MeV $\alpha$ particle than for MeV $\gamma$ quanta or relativistic charged particles.

For organic scintillators Birks [87] suggested a semi-empirical model describing the light-output degradation at high ionisation density $\mathrm{d}E/\mathrm{d}x$,

$$L = L_0 \frac{1}{1 + k_\mathrm{B} \cdot \mathrm{d}E/\mathrm{d}x} \ , \tag{5.56}$$

where $\mathrm{d}E/\mathrm{d}x$ is the ionisation loss in $\mathrm{MeV}/(\mathrm{g/cm^2})$ and $k_\mathrm{B}$ is *Birks' constant* which is characteristic for the scintillation material used. Typically, $k_\mathrm{B}$ is in the range $(1\text{–}5) \cdot 10^{-3}\,\mathrm{g}/(\mathrm{cm^2\,MeV})$.

*Gas scintillation counters* use light which is produced when charged particles excite atoms in interactions and these atoms subsequently decay into the ground state by light emission [87, 106]. The lifetime of the excited levels lies in the nanosecond range. Because of the low density, the light yield in gas scintillators is relatively low. However, liquid argon (LAr), krypton (LKr) and xenon (LXe) were found to be efficient scintillators [47, 107]. For example, the light output of liquid xenon is about the same as that of a NaI(Tl) crystal while the decay time is about 20 ns only. However, the maximum-emission wavelength is 174 nm (128 nm for LAr and 147 nm for LKr), which makes detection of this light very difficult, especially taking into account the necessity of the cryogenic environment.

The scintillation counter has to have high *light collection efficiency* and *uniform response* over its volume. To achieve this the light attenuation in a crystal should be small and the light attenuation length $\lambda_\mathrm{sc}$ becomes a very important characteristic of the scintillator.

Usually the scintillation light is collected from one or two faces of the counter by a photosensor surface $S_\mathrm{out}$, which is much smaller than the total surface $S_\mathrm{tot}$ of the counter. For counters of not too large size ($\approx 5$ cm or less) the best collection efficiency is obtained when all the surface except an output window is diffusively reflecting. A fine powder of magnesium oxide or porous Teflon film can be used as an effective reflector. For counters of approximately equal dimensions (e.g., close to spherical or cubic) the light collection efficiency $\eta_\mathrm{C}$ can be estimated by a simple formula (see Problem 5.4),

$$\eta_\mathrm{C} = \frac{1}{1 + \mu/q} \ , \tag{5.57}$$

https://doi.org/10.1017/9781009401531.008 Published online by Cambridge University Press

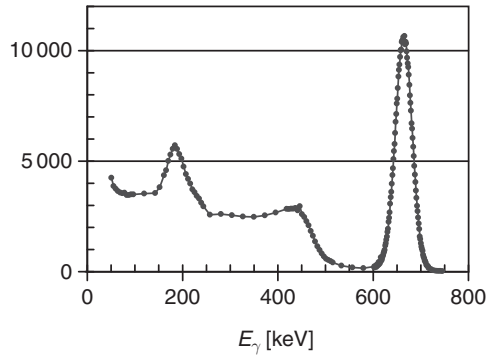


Fig. 5.26. Energy spectrum measured with a CsI(Tl) counter exposed to 662 keV $\gamma$ rays from a $^{137}$Cs radioactive source. The crystal of dimension $2 \cdot 2 \cdot 2\,\mathrm{cm}^3$ is viewed by a $1\,\mathrm{cm}^2$ silicon photodiode. The energy resolution, FWHM/$E_\gamma$, is about 6%.

where $q = S_{\mathrm{out}}/S_{\mathrm{tot}}$ and $\mu$ is the absorption coefficient for diffusive reflection. For crystals of medium size it is possible to reach $\mu \approx 0.05$–$0.02$ [108, 109], which provides a light collection efficiency of $\eta_{\mathrm{C}} \approx 60\%$–$70\%$.

Figure 5.26 shows a typical energy spectrum measured with a CsI(Tl) counter exposed to 662 keV $\gamma$ rays from a $^{137}$Cs radioactive source. The rightmost peak corresponds to full absorption of the photon (see Chap. 1), commonly called *photopeak*. The *Compton edge* at the end of the flat Compton continuum is to the left of the photopeak. Another peak observed at 184 keV is produced by photons backscattered from the surrounding material into the detector when they get absorbed by the photoelectric effect. The energy of this peak corresponds to the difference between full absorption and the Compton edge. The energy resolution is dominated by statistical fluctuations of the number of photoelectrons, $N_{\mathrm{pe}}$, generated in the photosensor by the scintillation light and by electronics noise. The number of photoelectrons, $N_{\mathrm{pe}}$, can be calculated from

$$N_{\mathrm{pe}} = L_{\mathrm{ph}} \cdot E_{\mathrm{dep}} \cdot \eta_{\mathrm{C}} \cdot Q_{\mathrm{s}} \ , \tag{5.58}$$

where $E_{\mathrm{dep}}$ is the deposited energy, $L_{\mathrm{ph}}$ the number of light photons per 1 MeV of energy absorbed in the scintillator, $\eta_{\mathrm{C}}$ the light collection efficiency, and $Q_{\mathrm{s}}$ the quantum efficiency of the photosensor. Then the energy resolution is given by the formula

$$\sigma_{E_{\mathrm{dep}}}/E_{\mathrm{dep}} = \sqrt{\frac{f}{N_{\mathrm{pe}}} + \left(\frac{\sigma_{\mathrm{e}}}{E_{\mathrm{dep}}}\right)^2 + \Delta^2} \ . \tag{5.59}$$

https://doi.org/10.1017/9781009401531.008 Published online by Cambridge University Press

Here $f$ is the so-called 'excess noise factor' describing the statistical fluctuations introduced by the photosensor, $\sigma_e$ is the noise of the read-out electronics, and $\Delta$ stands for other contributions like non-linear scintillator response, non-uniformity of the light collection, etc.

For scintillation counters of large sizes, especially having the shape of long bars or sheets, the optimal way of light collection is to use the effect of internal (total) reflection. To achieve this all surfaces of the scintillator must be carefully polished. Let us consider a scintillator of parallelepiped-like shape with a photosensor attached to one of its faces with perfect optical contact. The light that does not fulfil the condition of internal reflection leaves the counter through one of the five faces while the remaining light is collected by the photosensor. Assuming an uniform angular distribution of scintillation photons, the amount of light leaving the scintillator through each face is given by the formula

$$\frac{\Delta I}{I_{\mathrm{tot}}} = \frac{1-\cos\beta_{\mathrm{ir}}}{2} = \frac{1}{2}\left(1-\sqrt{1-\frac{1}{n^2}}\right) \quad , \tag{5.60}$$

where $\beta_{\mathrm{ir}}$ is the angle for internal reflection, $n$ the index of refraction of the scintillator, $I_{\mathrm{tot}}$ the total surface area of the counter, and $\Delta I$ the area of one of the faces. Then the light collection efficiency is

$$\eta_{\mathrm{C}} = 1 - 5 \cdot \frac{\Delta I}{I_{\mathrm{tot}}} \quad . \tag{5.61}$$

For counters of large size the loss of scintillation light due to bulk absorption or surface scattering is not negligible. High-quality scintillators have light attenuation lengths including both effects of about 2 m.

Normally large-area scintillators are read out with several photomultipliers. The relative pulse heights of these photomultipliers can be used to determine the particle's point of passage and thereby enable a correction of the measured light yield for absorption effects.

Plastic scintillators used in detectors are usually in the form of scintillator plates. The scintillation light emerges from the edges of these plates and has to be guided to a photomultiplier and also matched to the usually circular geometry of the photosensing device. This matching is performed with *light guides*. In the most simple case (Fig. 5.27) the light

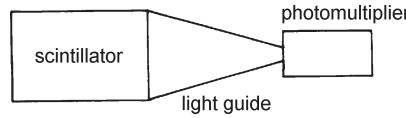


Fig. 5.27. Light readout with a 'fish-tail' light guide.

https://doi.org/10.1017/9781009401531.008 Published online by Cambridge University Press

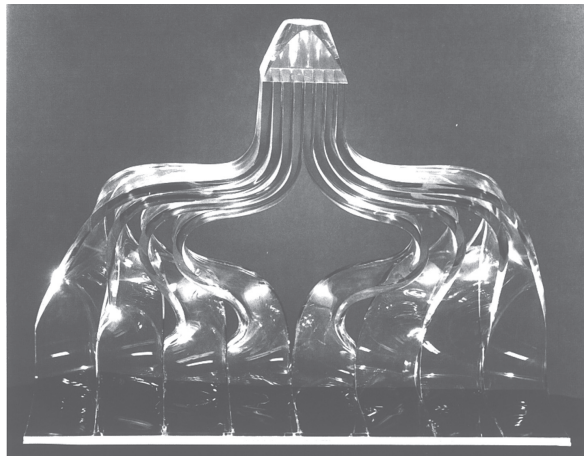

Fig. 5.28. Photograph of an adiabatic light guide [110].

is transferred via a triangular light guide (*fish-tail*) to the photocathode of a photomultiplier. A complete light transfer, i.e. light transfer without any losses, using fish-tail light guides is impossible. Only by using complicated light guides can the end face of a scintillator plate be imaged onto the photocathode without appreciable loss of light (*adiabatic light guides*). Figure 5.28 shows the working principle of an adiabatic light guide ($dQ = 0$, i.e. no loss of light). Individual parts of the light-guide system can be only moderately bent because otherwise the light, which is normally contained in the light guide by internal reflection, will be lost at the bends.

The scintillator end face cannot be focussed without light loss onto a photocathode with a smaller area because of *Liouville's theorem*, which states: 'The volume of an arbitrary phase space may change its form in the course of its temporal and spatial development, its size, however, remains constant.'

## 5.5 Photomultipliers and photodiodes

The most commonly used instrument for the measurement of fast light signals is the *photomultiplier* (PM). Light in the visible or ultraviolet range – e.g. from a scintillation counter – liberates electrons from a photocathode via the photoelectric effect. For particle detectors photomultipliers with a semi-transparent photocathode are commonly used. This photocathode is a very thin layer of a semiconductor compound (SbCs, SbKCs, SbRbKCs and others) deposited to the interior surface of the transparent input window.

https://doi.org/10.1017/9781009401531.008 Published online by Cambridge University Press

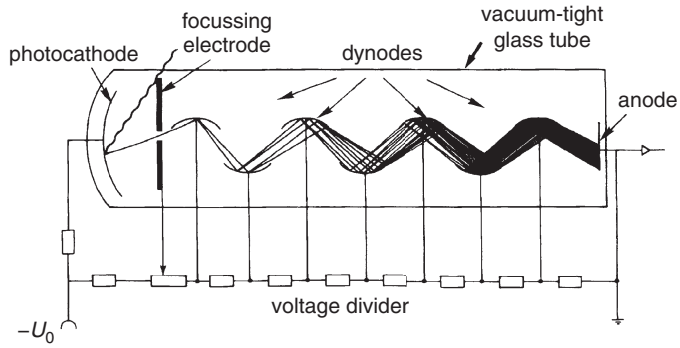


Fig. 5.29. Working principle of a photomultiplier. The electrode system is mounted in an evacuated glass tube. The photomultiplier is usually shielded by a mu-metal cylinder made from high-permeability material against stray magnetic fields (e.g. the magnetic field of the Earth).

For most counters a negative high voltage is applied to the photocathode, although for some types of measurements the opposite way (where a positive high voltage is applied to the anode) is recommended. Photoelectrons are focussed by an electric guiding field onto the first dynode, which is part of the multiplication system. The anode is normally at ground potential. The voltage between the photocathode and anode is subdivided by a chain of resistors. This voltage divider supplies the dynodes between the photocathode and anode so that the applied negative high voltage is subdivided linearly (Fig. 5.29). Detailed descriptions of photomultiplier operation and applications can be found in [111, 112].

An important parameter of a photomultiplier is its *quantum efficiency*, i.e. the mean number of photoelectrons produced per incident photon. For the most popular bialkali cathodes (Cs–K with Sb) the quantum efficiency reaches values around 25% for a wavelength of about 400 nm. It is worth to note that in the last years photomultiplier tubes with GaAs and GaInAsP photocathodes having quantum efficiencies up to 50% became commercially available. However, these devices are up to now not in frequent use and they do have some limitations.

Figure 5.30 shows the quantum efficiency for bialkali cathodes as a function of the wavelength [111]. The quantum efficiency decreases for short wavelengths because the transparency of the photomultiplier window decreases with increasing frequency, i.e. shorter wavelength. The range of efficiency can only be extended to shorter wavelengths by using UV-transparent quartz windows.

The dynodes must have a high *secondary-electron emission coefficient* (BeO or Mg–O–Cs). For electron energies from around 100 eV up to 200 eV, which correspond to typical acceleration voltages between

https://doi.org/10.1017/9781009401531.008 Published online by Cambridge University Press

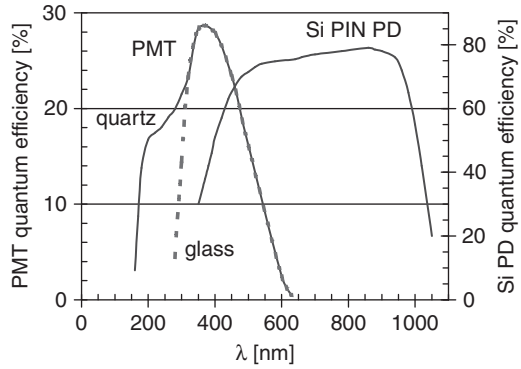


Fig. 5.30. Quantum efficiency of a bialkali cathode as function of the wavelength [111] in comparison to a silicon PIN photodiode [113]. Note that the quantum efficiencies for the photomultiplier and the silicon photodiode are marked with different scales at opposite sides of the figure.

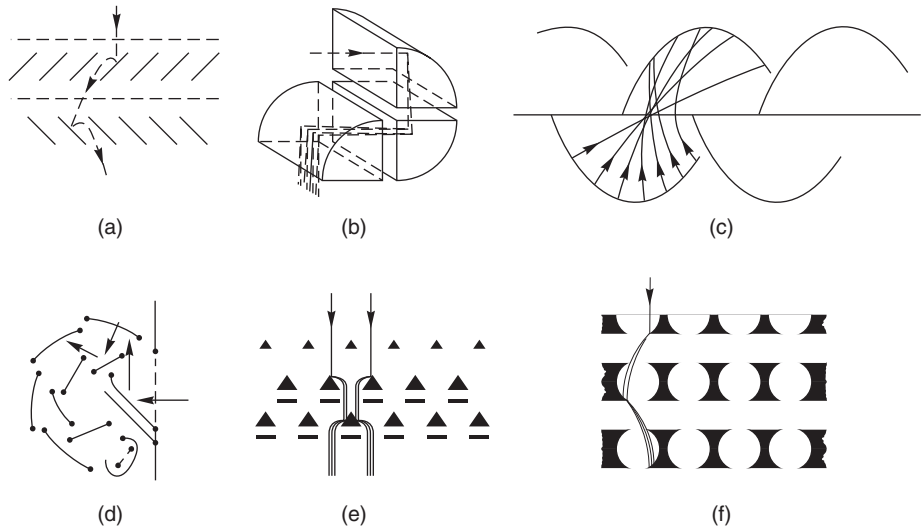


Fig. 5.31. Some dynode system configurations: (a) venetian blind, (b) box, (c) linear focussing, (d) circular cage, (e) mesh and (f) foil [111].

two dynodes, approximately three to five secondary electrons are emitted [111]. Various types of geometries for dynode systems are shown in Fig. 5.31. For an $n$-dynode photomultiplier with a secondary emission coefficient $g$, the current amplification is given by

$$A = g^n \ . \tag{5.62}$$

https://doi.org/10.1017/9781009401531.008 Published online by Cambridge University Press

For typical values of $g = 4$ and $n = 12$ one obtains $A = 4^{12} \approx 1.7 \cdot 10^7$.

The charge arriving at the anode for one photoelectron,

$$Q = eA \approx 2.7 \cdot 10^{-12}\,\mathrm{C}\ , \tag{5.63}$$

is collected within approximately 5 ns leading to an anode current of

$$i = \frac{\mathrm{d}Q}{\mathrm{d}t} \approx 0.5\,\mathrm{mA}\ . \tag{5.64}$$

If the photomultiplier is terminated with a $50\,\Omega$ resistor, a voltage signal of

$$\Delta U = R \cdot \frac{\mathrm{d}Q}{\mathrm{d}t} \approx 27\,\mathrm{mV} \tag{5.65}$$

is obtained.

Thus one photoelectron can be firmly detected. Figure 5.32 shows the pulse-height distribution for a single-photoelectron signal of a photomultiplier with a linear-focussing dynode system. The ratio of the maximum and minimum values of this distribution is called 'peak-to-valley ratio' and reaches about 3. The peak width is mostly determined by the Poisson statistics of the secondary electrons emitted from the first dynode. The left part of the spectrum is caused by the thermoemission from the first dynode and from electronics noise.

The contribution of the photomultiplier to the overall counter energy resolution is determined by photoelectron statistics, non-uniformity of the quantum efficiency and photoelectron collection efficiency over the photocathode, and the excess noise factor $f$, see Eq. (5.59). The term $\Delta$

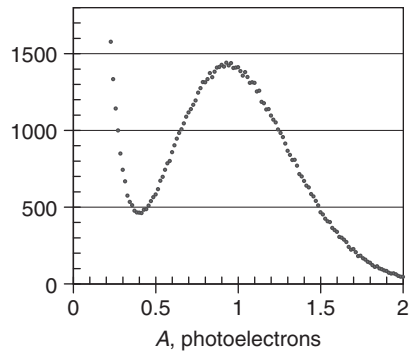


Fig. 5.32. Anode pulse distribution for a single-photoelectron signal for a photomultiplier with a linear-focussing dynode system.

https://doi.org/10.1017/9781009401531.008 Published online by Cambridge University Press

is usually negligible for photomultiplier tubes. The excess noise factor for a photomultiplier is given by

$$f = 1 + \frac{1}{g_1} + \frac{1}{g_1 g_2} + \cdots + \frac{1}{g_1 g_2 \cdots g_n} \approx 1 + \frac{1}{g_1} \ , \tag{5.66}$$

where $g_i$ is the gain at the $i$th dynode.

The *rise time* of the photomultiplier signal is typically 1–3 ns. This time has to be distinguished from the time required for electrons to traverse the photomultiplier. This *transit time* depends on the phototube type and varies typically from 10 ns to 40 ns.

The *time jitter* in the arrival time of electrons at the anode poses a problem for reaching a high time resolution. Two main sources of the time jitter are the variation in the velocity of the photoelectrons and the difference of the path lengths from the production point of the photoelectrons to the first dynode which can be subject to large fluctuations.

The time jitter (or transit-time spread, TTS) caused by different velocities of photoelectrons can easily be estimated. If $s$ is the distance between photocathode and the first dynode, then the time $t_1$ when an electron with initial kinetic energy $T$ reaches the first dynode can be found from the expression

$$s = \frac{1}{2}\frac{eE}{m}t_1^2 + t_1 \cdot \sqrt{2T/m} \ , \tag{5.67}$$

where $E$ is the electric field strength and $m$ the electron mass. Then one can estimate the difference between $t_1$ for photoelectrons at $T = 0$ and those with an average kinetic energy $T$,

$$\delta t = \frac{\sqrt{2mT}}{eE} \ . \tag{5.68}$$

For $T = 1\,\mathrm{eV}$ and $E = 200\,\mathrm{V/cm}$ a time jitter of $\delta t = 0.17\,\mathrm{ns}$ is obtained. For a fast XP2020 PM tube with 50 mm photocathode diameter this spread is $\sigma_{\mathrm{TTS}} = 0.25\,\mathrm{ns}$ [114]. The arrival-time difference based on path-length variations strongly depends on the size and shape of the photocathode. For an XP4512 phototube with planar photocathode and a cathode diameter of 110 mm this time difference amounts to $\sigma_{\mathrm{TTS}} = 0.8\,\mathrm{ns}$ in comparison to 0.25 ns for an XP2020 [114].

For large photomultipliers the achievable time resolution is limited essentially by path-length differences. The photomultipliers with a 20-inch cathode diameter used in the Kamiokande nucleon decay and neutrino experiment [115, 116] show path-length differences of up to 5 ns. For this phototube the distance between photocathode and first dynode is so large that the Earth's magnetic field has to be well shielded so that the

https://doi.org/10.1017/9781009401531.008 Published online by Cambridge University Press

Fig. 5.33. Photograph of an 8-inch photomultiplier (type R 4558) [117].

photoelectrons can reach the first dynode. Figure 5.33 shows a photograph of an 8-inch photomultiplier [117].

To obtain position sensitivity, the anode of a photomultiplier tube can be subdivided into many independent pads or it can be built as a set of strips (or two layers of crossed strips) [112]. To preserve the position information the dynode system has to transfer the image from the photocathode with minimal distortions. To meet this condition, the dynode system of this device should be placed very close to the cathode. It can be made as a set of layers of fine mesh or foils. The anode pixel size can be $2 \times 2\,\mathrm{mm}^2$ at a pitch of 2.5 mm. Such photomultiplier tubes are used in gamma cameras for medical applications [118] as well as in high energy physics experiments [119, 120].

The path-length fluctuations can be significantly reduced in photomultipliers (*channel plates*) with microchannel plates as multiplication system (MCP-PMT). The principle of operation of such channel plates is shown in Fig. 5.34 [112]. A voltage of about 1000 V is applied to a thin glass tube (diameter 6–50 µm, length 1–5 mm) which is coated on the inside with a resistive layer. Incident photons produce photoelectrons on a photocathode or on the inner wall of the microchannel. These are, like in the normal phototube, multiplied at the – in this case – continuous dynode. Channel plates contain a large number ($10^4$ to $10^7$) of such channels which are implemented as holes in a lead-glass plate. A microphotographic record of such channels with a diameter of 12.5 µm [121] is shown in Fig. 5.34. A photomultiplier tube with a single MCP provides a gain up to $10^3$–$10^4$. To obtain a higher gain, two or three MCP in series can be incorporated into the MCP-PMT.

https://doi.org/10.1017/9781009401531.008 Published online by Cambridge University Press

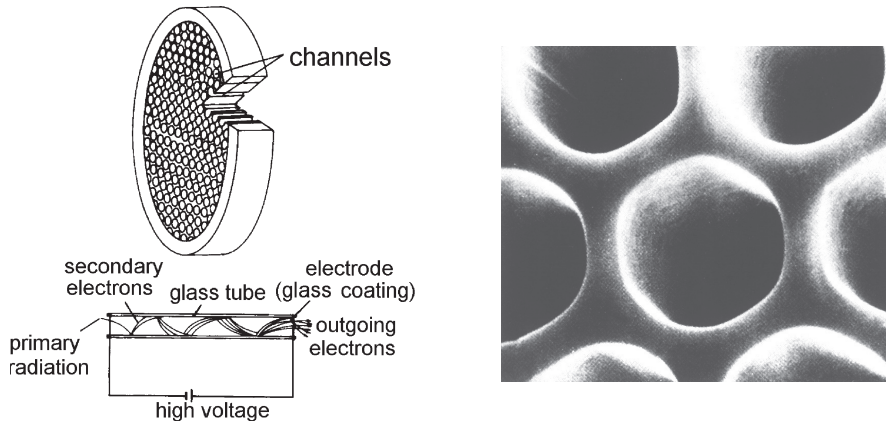


Fig. 5.34. Working principle of a channel plate [112] (left) and microphotograph of microchannels (right) [121].

Because of the short mean path lengths of electrons in the longitudinal electric field, path-length fluctuations are drastically reduced compared to a normal photomultiplier. Transit-time differences of about 30 ps for multiplication factors between $10^5$ and $10^6$ are obtained [122].

While normal photomultipliers practically cannot be operated in magnetic fields (or if so, only heavily shielded), the effect of magnetic fields on channel plates is comparatively small. This is related to the fact that in channel plates the distance between cathode and anode is much shorter. There are, however, recent developments of conventional photomultipliers with transparent wire-mesh dynodes, which can withstand moderate magnetic fields.

A problem with channel plates is the flux of positive ions produced by electron collisions with the residual gas in the channel plate that migrate in the direction of the photocathode. The lifetime of channel plates would be extremely short if the positive ions were not prevented from reaching the photocathode. By use of extremely thin aluminium windows of $\approx$ 7 nm thickness (transparent for electrons) mounted between photocathode and channel plate, the positive ions are absorbed. In this way, the photocathode is shielded against the ion bombardment.

A very promising photosensor is the hybrid photomultiplier tube (HPMT) [123, 124]. This device has only a photocathode and a silicon PIN diode as an anode. A high voltage, up to 15–20 kV, is applied to the gap between the photocathode and PIN diode. The diode of 150–300 µm thickness is fully depleted under reverse-bias voltage. Photoelectrons accelerated by the electric field penetrate a very thin (about 500 Å) upper contact layer, get to the depleted area, and produce multiple electron–hole pairs. The gain of this device can reach 5000. Figure 5.35

https://doi.org/10.1017/9781009401531.008 Published online by Cambridge University Press

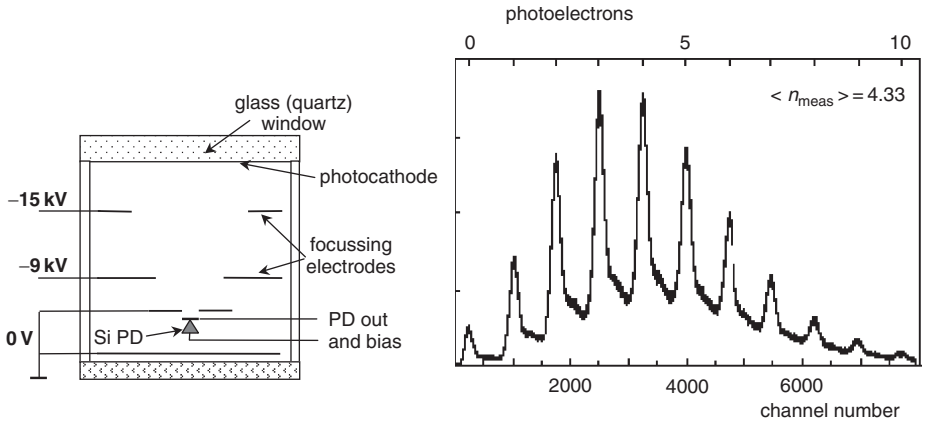


Fig. 5.35. The layout of the hybrid PMT and the amplitude spectrum measured with light flashes from scintillation fibres. Each peak corresponds to a certain number of photoelectrons emerging from the photocathode [125].

shows the layout of a HPMT and the amplitude spectrum of light flashes measured with a HPMT [125]. The peaks which correspond to signals with a certain number of photoelectrons are distinctively seen (compare with Fig. 5.32 for a usual PM tube).

Recent developments of modern electronics made it possible to use low-gain photosensors for particle detectors. These are one- or two-dynode PM tubes (*phototriodes* and *phototetrodes*) [126–128] as well as *silicon photodiodes*. The main reasons to use these devices are their low sensitivity or insensitivity to magnetic fields, their compactness, better stability and lower price.

Semiconductor photodetectors are known for a long time and the possibility to use silicon photodiodes (PD) for particle detection in combination with large-size scintillation crystals CsI(Tl), NaI(Tl), BGO was demonstrated in 1982–5 [129, 130].

The main operation principles as well as the structure of PIN photodiodes are very similar to that for a silicon particle detector described in Sect. 5.3 (see Fig. 5.19). The difference is that the layers in front of the depletion region should be transparent for the light to be detected. A photodiode contains a very thin layer of highly doped $p^+$ silicon followed by a layer of moderately doped $n$-Si of 200–500 μm thickness (called $i$ layer) and ending with a highly doped $n^+$-Si layer. A $SiO_2$ film is mounted on top of the $p^+$ layer. The whole structure is attached to a ceramic substrate and covered with a transparent window.

The photon enters the depletion area, penetrates to the $i$ layer where the bias voltage $U_b$ is applied, and creates an electron–hole pair that is separated by the electric field which exists in this area.

https://doi.org/10.1017/9781009401531.008 Published online by Cambridge University Press

The photodiode signal is usually read out by a charge-sensitive preamplifier (CSPA) followed by a shaping amplifier with optimal filtering (see Chap. 14). The electronics noise of such a chain is usually characterised by the equivalent noise charge described as (see also Sect. 14.9)

$$\sigma_Q = \sqrt{2eI_{\mathrm{D}}\tau + a\tau + \frac{b}{\tau}(C_{\mathrm{p}} + C_{\mathrm{fb}})^2} \ , \tag{5.69}$$

where $\tau$ is the shaping time, $I_{\mathrm{D}}$ the photodiode dark current, $a$ the contribution of parallel noise of the input preamplifier chain, $b$ describes the thermal noise, $C_{\mathrm{p}}$ the photodiode capacity and $C_{\mathrm{fb}}$ the feedback capacity.

As can be seen from this formula, the noise level depends crucially on the total capacity at the CSPA input. To reduce the photodiode capacity, the depletion layer should be extended. On the other hand, the photodiode dark current is related to the electron–hole pairs produced in the depletion layer by thermal excitation. Hence the dark current should be proportional to the depleted-area volume (in reality part of this current is due to a surface component). At present, photodiodes used for particle detectors have an area of 0.5–4 $\mathrm{cm}^2$ and $i$-layer thicknesses of 200–500 $\mu$m. The dark current of these devices is 0.5–3 $\mathrm{nA/cm}^2$ while the capacity is about 50 $\mathrm{pF/cm}^2$.

A specific feature of the semiconductor photodiode performance is the so-called *nuclear counter effect*, i.e. the possibility of electron–hole production not only by photons but also by charged particles crossing the *pn* junction. This effect should be taken into account when designing a detector system using photodiodes. On the other hand, X-ray absorption provides an opportunity for a direct counter calibration. For that we can irradiate a photodiode by X rays of known energy from a radioactice source, e.g. $^{241}$Am. An example of such a spectrum is presented in Fig. 5.36. The number of electron–hole pairs corresponding to the 60 keV peak is easily calculated taking into account $W_{\mathrm{Si}} = 3.65$ eV.

Since the operation principles of a solid-state ionisation counter are similar to a gaseous one, it is a natural idea to use photodiodes in the proportional mode. The first successful devices of this type, suitable for usage in scintillation counters, were developed in 1991–3 [131–133]. At present, these avalanche photosensors are used rather widely [134].

The principle of operation of *avalanche photodiodes* (APDs) is illustrated in Fig. 5.37. This device has a complex doping profile which provides a certain area with high electric field. Photons penetrate several microns into a *p*-silicon layer before they create an electron–hole pair. A weak electric field existing in this area separates the pair and causes the electrons to drift to the *pn* junction which exhibits a very high field strength. Here the electron can gain enough energy to create new

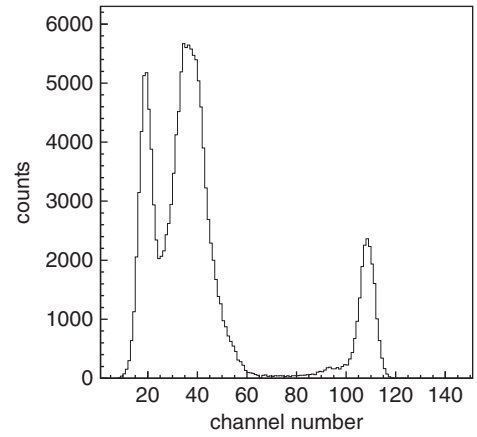


Fig. 5.36. Pulse-height distribution taken with a 1 cm$^2$ Si photodiode at room temperature exposed to X rays from an $^{241}$Am source. The rightmost peak corresponds to photons of 60 keV energy while the second, broad peak results from an overlap of further non-resolved $\gamma$-ray and X-ray lines in the range of 15–30 keV. For details see also Appendix 5, Fig. A5.10.

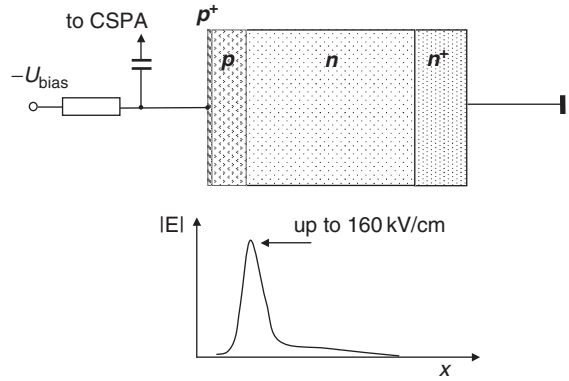


Fig. 5.37. The layout of an avalanche photodiode together with the electric field-strength distribution.

electron–hole pairs. Due to impact ionisation such a device can provide an amplification of up to 1000 for existing avalanche photodiodes.

Since the avalanche multiplication is a statistical process, the statistical fluctuation of the collected charge is higher than that determined from the Poisson spread of the number of initial photons, $\sigma = \sqrt{f/n}$, where $f$ is the 'excess noise factor'.

https://doi.org/10.1017/9781009401531.008 Published online by Cambridge University Press

As first approximation, the equivalent noise charge $\sigma_q$ is expressed by

$$\sigma_q^2 = 2e\left(\frac{I_{\rm ds}}{M^2} + I_{\rm db} f\right)\tau + 4kTR_{\rm en}\frac{C_{\rm tot}^2}{M^2}\frac{1}{\tau} \ , \tag{5.70}$$

where $M$ is the avalanche multiplication coefficient, $I_{\rm ds}$ the dark-current component caused by surface leakage, $I_{\rm db}$ the bulk dark-current component, $\tau$ the shaping time, $R_{\rm en}$ the equivalent noise resistance of the amplifier and $C_{\rm tot}$ the total input capacity (see also Sect. 14.9).

It is clear from Eq. (5.70) that the surface dark current does not give a significant contribution to the equivalent noise charge due to the large factor $M$ in the denominator. The bulk dark current is normally quite low due to the thin $p$ layer in front of the avalanche amplification region.

Let us consider the simplest APD model assuming that an avalanche occurs in a uniform electric field in a layer $0 < x < d$. Both electrons and holes can produce new pairs but the energy threshold for holes is much higher due to their larger effective mass. Denoting the probabilities of ionisation per unit drift length as $\alpha_e$ and $\alpha_p$, respectively, we arrive at the following equations for electron ($i_e$) and hole ($i_p$) currents:

$$\frac{{\rm d}i_e(x)}{{\rm d}x} = \alpha_e i_e(x) + \alpha_p i_p(x) \ , \ \ i_e(x) + i_p(x) = i_{\rm tot} = {\rm const} \ . \tag{5.71}$$

The solution of these equations for the initial conditions

$$i_e(0) = i_0 \ , \ \ i_p(d) = 0 \tag{5.72}$$

leads to an amplification of

$$M = \frac{i_{\rm tot}}{i_0} = \left(1 - \frac{\alpha_p}{\alpha_e}\right)\frac{1}{{\rm e}^{-(\alpha_e - \alpha_p)d} - \frac{\alpha_p}{\alpha_e}} \ . \tag{5.73}$$

The quantities $\alpha_e$ and $\alpha_p$ are analogues of the first Townsend coefficient (see Sect. 5.1.2), and they increase with increasing field strength. The gain rises according to Eq. (5.73). When $\alpha_p$ becomes sufficiently high to fulfil the condition

$${\rm e}^{-(\alpha_e - \alpha_p)d} = \frac{\alpha_p}{\alpha_e} \ , \tag{5.74}$$

the APD will break down.

The gain and dark current in their dependence on the bias voltage for a $5 \times 5\,{\rm mm}^2$ APD produced by 'Hamamatsu Photonics' are shown in Fig. 5.38a. The noise level versus gain is presented in Fig. 5.38b.

In the bias-voltage range where $\alpha_p \ll \alpha_e$, the APD can be considered as a multistage multiplier with a multiplication coefficient at each stage

https://doi.org/10.1017/9781009401531.008 Published online by Cambridge University Press

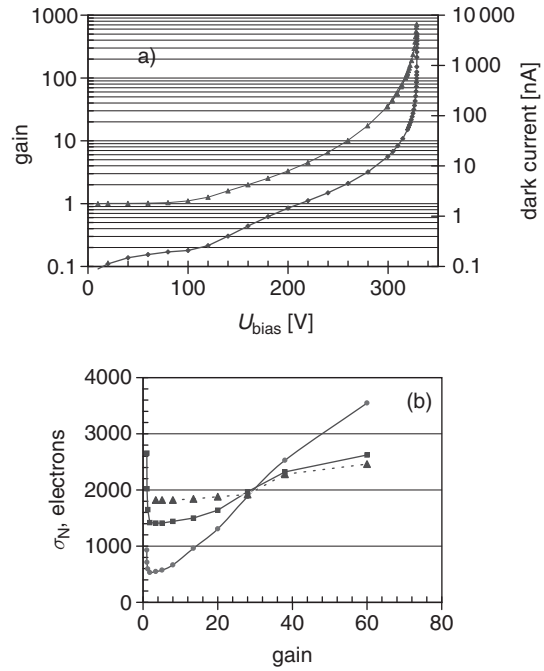


Fig. 5.38. (a) The gain (▲) and dark current (♦) in their dependence on the bias voltage for a $5 \times 5\,\mathrm{mm}^2$ APD produced by 'Hamamatsu Photonics'; (b) The noise level versus gain for different shaping times: 2 µs (●), 0.25 µs (■) and 0.1 µs (▲).

equal to 2. For this case one can derive a value for the excess noise factor of $f = 2$.

A more detailed theory of processes in APDs was developed in [135, 136]. This theory gives an expression for the excess noise factor of

$$f = K_{\mathrm{eff}} M + (2 - 1/M)(1 - K_{\mathrm{eff}}) \ , \tag{5.75}$$

where $K_{\mathrm{eff}}$ is a constant on the order of 0.01.

Avalanche photodiodes have two important advantages in comparison to photodiodes without amplification: a much lower nuclear counter effect and a much higher radiation tolerance [133, 134]. Both of these features originate from the small thickness of the $p$ layer in front of the avalanche area. The quantum efficiency of an APD is basically close to that for a normal PIN photodiode.

When the bias voltage approaches the breakdown threshold, the APD reaches a regime similar to the Geiger mode (see Sect. 5.1.3). As in the Geiger regime the output signals do not depend on the amount of light at the input, but rather are limited by the resistance and capacity of the device. However, this mode became the basis for another promising

https://doi.org/10.1017/9781009401531.008 Published online by Cambridge University Press

photosensor – the so-called *silicon photomultiplier*. Such a device consists of a set of pixel Geiger APDs with a size of 20–50 μm built on a common substrate with the total area of 0.5–1 $mm^2$. When the total number of photons in a light flash is not too large, the output pulse is proportional to this number with a multiplication coefficient of $\approx 10^6$ [137].

## 5.6 Cherenkov counters

A charged particle, traversing a medium with refractive index $n$ with a velocity $v$ exceeding the velocity of light $c/n$ in that medium, emits a characteristic electromagnetic radiation, called Cherenkov radiation [138, 139]. Cherenkov radiation is emitted because the charged particle polarises atoms along its track so that they become electric dipoles. The time variation of the dipole field leads to the emission of electromagnetic radiation. As long as $v < c/n$, the dipoles are symmetrically arranged around the particle path, so that the dipole field integrated over all dipoles vanishes and no radiation occurs. If, however, the particle moves with $v > c/n$, the symmetry is broken resulting in a non-vanishing dipole moment, which leads to the radiation. Figure 5.39 illustrates the difference in polarisation for the cases $v < c/n$ and $v > c/n$ [140, 141].

The contribution of Cherenkov radiation to the energy loss is small compared to that from ionisation and excitation, Eq. (1.11), even for minimum-ionising particles. For gases with $Z \geq 7$ the energy loss by Cherenkov radiation amounts to less than 1% of the ionisation loss of minimum-ionising particles. For light gases (He, H) this fraction amounts to about 5% [21, 22].

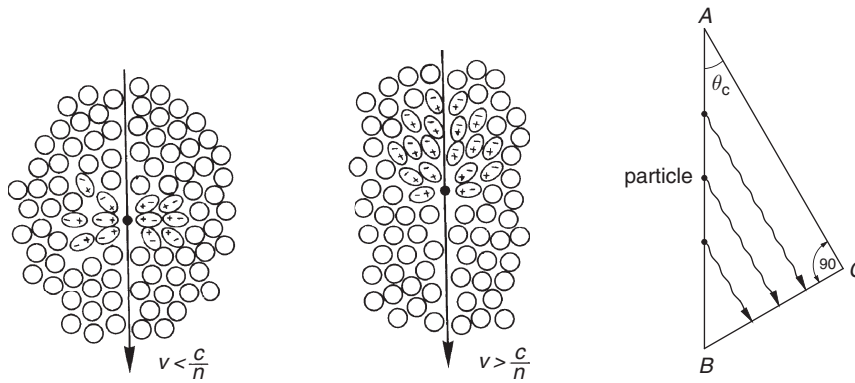


Fig. 5.39. Illustration of the Cherenkov effect [140, 141] and geometric determination of the Cherenkov angle.

https://doi.org/10.1017/9781009401531.008 Published online by Cambridge University Press

The angle between the emitted Cherenkov photons and the track of the charged particle can be obtained from a simple argument (Fig. 5.39). While the particle has travelled the distance $AB = t\beta c$, the photon has advanced by $AC = t \cdot c/n$. Therefore one obtains

$$\cos\theta_{\mathrm{c}} = \frac{c}{n\beta c} = \frac{1}{n\beta} \ . \tag{5.76}$$

For the emission of Cherenkov radiation there is a *threshold effect*. Cherenkov radiation is emitted only if $\beta > \beta_{\mathrm{c}} = \frac{1}{n}$. At threshold, Cherenkov radiation is emitted in the forward direction. The *Cherenkov angle* increases until it reaches a maximum for $\beta = 1$, namely

$$\theta_{\mathrm{c}}^{\max} = \arccos\frac{1}{n} \ . \tag{5.77}$$

Consequently, Cherenkov radiation of wavelength $\lambda$ requires $n(\lambda) > 1$. The maximum emission angle, $\theta_{\mathrm{c}}^{\max}$, is small for gases ($\theta_{\mathrm{c}}^{\max} \approx 1.4°$ for air) and becomes large for condensed media (about 45° for usual glass).

For fixed energy, the threshold Lorentz factor depends on the mass of the particle. Therefore, the measurement of Cherenkov radiation is well suited for particle-identification purposes.

The number of Cherenkov photons emitted per unit path length with wavelengths between $\lambda_1$ and $\lambda_2$ is given by

$$\frac{\mathrm{d}N}{\mathrm{d}x} = 2\pi\alpha z^2 \int_{\lambda_1}^{\lambda_2} \left(1 - \frac{1}{(n(\lambda))^2\beta^2}\right) \frac{\mathrm{d}\lambda}{\lambda^2} \ , \tag{5.78}$$

for $n(\lambda) > 1$, where $z$ is the electric charge of the particle producing Cherenkov radiation and $\alpha$ is the fine-structure constant.

Neglecting the dispersion of the medium (i.e. $n$ independent of $\lambda$) leads to

$$\frac{\mathrm{d}N}{\mathrm{d}x} = 2\pi\alpha z^2 \cdot \sin^2\theta_{\mathrm{c}} \cdot \left(\frac{1}{\lambda_1} - \frac{1}{\lambda_2}\right) \ . \tag{5.79}$$

For the optical range ($\lambda_1 = 400\,\mathrm{nm}$ and $\lambda_2 = 700\,\mathrm{nm}$) one obtains for singly charged particles ($z = 1$)

$$\frac{\mathrm{d}N}{\mathrm{d}x} = 490\ \sin^2\theta_{\mathrm{c}}\,\mathrm{cm}^{-1} \ . \tag{5.80}$$

Figure 5.40 shows the number of Cherenkov photons emitted per unit path length for various materials as a function of the velocity of the particle [142].

The photon yield can be increased by up to a factor of two or three if the photons emitted in the ultraviolet range can also be detected. Although

https://doi.org/10.1017/9781009401531.008 Published online by Cambridge University Press

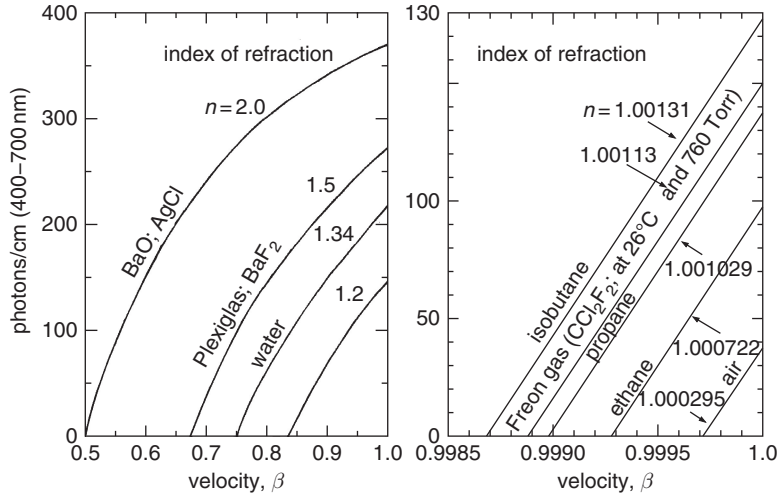


Fig. 5.40. Number of produced Cherenkov photons per unit path length for various materials as a function of the particle velocity [142].

the spectrum of emitted Cherenkov photons exhibits a $1/\lambda^2$ dependence, see Eq. (5.78), Cherenkov photons are not emitted in the X-ray range because in this region the index of refraction is $n = 1$, and therefore the condition for Cherenkov emission cannot be fulfilled.

To obtain the correct number of photons produced in a Cherenkov counter, Eq. (5.78) must be integrated over the region for which $\beta \cdot n(\lambda) > 1$. Also the response function of the light collection system must be taken into account to obtain the number of photons arriving at the photon detector.

All transparent materials are candidates for Cherenkov radiators. In particular, Cherenkov radiation is emitted in all scintillators and in the light guides which are used for the readout. The scintillation light, however, is approximately 100 times more intense than the Cherenkov light. A large range of indices of refraction can be covered by the use of solid, liquid or gaseous radiators (Table 5.4).

Ordinary liquids have indices of refraction greater than $\approx 1.33$ ($H_2O$) and gases have $n$ less than about 1.002 (pentane). Although gas Cherenkov counters can be operated at high pressure, thus increasing the index of refraction, the substantial gap between $n = 1.33$ and $n = 1.002$ cannot be bridged in this way.

By use of *silica aerogels*, however, it has become feasible to cover this missing range of the index of refraction. Aerogels are phase mixtures from $m$ ($SiO_2$) and $2m$ ($H_2O$) where $m$ is an integer. Silica aerogels form a porous structure with pockets of air. The diameter of the air bubbles

https://doi.org/10.1017/9781009401531.008 Published online by Cambridge University Press

Table 5.4. *Compilation of Cherenkov radiators [1, 143]. The index of refraction for gases is for 0 °C and 1 atm (STP). Solid sodium is transparent for wavelengths below 2000 Å [144, 145]*

| Material | $n-1$ | $\beta$ threshold | $\gamma$ threshold |
|---|---|---|---|
| Solid sodium | 3.22 | 0.24 | 1.029 |
| Diamond | 1.42 | 0.41 | 1.10 |
| Flint glass (SFS1) | 0.92 | 0.52 | 1.17 |
| Lead fluoride | 0.80 | 0.55 | 1.20 |
| Aluminium oxide | 0.76 | 0.57 | 1.22 |
| Lead glass | 0.67 | 0.60 | 1.25 |
| Polystyrene | 0.60 | 0.63 | 1.28 |
| Plexiglas (Lucite) | 0.48 | 0.66 | 1.33 |
| Borosilicate glass (Pyrex) | 0.47 | 0.68 | 1.36 |
| Lithium fluoride | 0.39 | 0.72 | 1.44 |
| Water | 0.33 | 0.75 | 1.52 |
| Liquid nitrogen | 0.205 | 0.83 | 1.79 |
| Silica aerogel | 0.007–0.13 | 0.993–0.884 | 8.46−2.13 |
| Pentane (STP) | $1.7 \cdot 10^{-3}$ | 0.9983 | 17.2 |
| $CO_2$ (STP) | $4.3 \cdot 10^{-4}$ | 0.9996 | 34.1 |
| Air (STP) | $2.93 \cdot 10^{-4}$ | 0.9997 | 41.2 |
| $H_2$ (STP) | $1.4 \cdot 10^{-4}$ | 0.99986 | 59.8 |
| He (STP) | $3.3 \cdot 10^{-5}$ | 0.99997 | 123 |

in the aerogel is small compared to the wavelength of the light so that the light 'sees' an average index of refraction between the air and the solid forming the aerogel structure. Silica aerogels can be produced with densities between $0.1\,\mathrm{g/cm^3}$ and $0.6\,\mathrm{g/cm^3}$ [1, 101, 146] and indices of refraction between 1.01 and 1.13. There is a simple relation between the aerogel density (in $\mathrm{g/cm^3}$) and the index of refraction [147, 148]:

$$n = 1 + 0.21 \cdot \varrho \ [\mathrm{g/cm^3}] \ . \tag{5.81}$$

The Cherenkov effect is used for particle identification in threshold detectors as well as in detectors which exploit the angular dependence of the radiation. These *differential Cherenkov counters* provide in fact a direct measurement of the particle velocity. The working principle of a differential Cherenkov counter which accepts only particles in a certain velocity range is shown in Fig. 5.41 [4, 149–151].

All particles with velocities above $\beta_{\min} = 1/n$ are accepted. With increasing velocity the Cherenkov angle increases and finally reaches the critical angle for internal reflection, $\theta_\mathrm{t}$, in the radiator so that no light can

https://doi.org/10.1017/9781009401531.008 Published online by Cambridge University Press

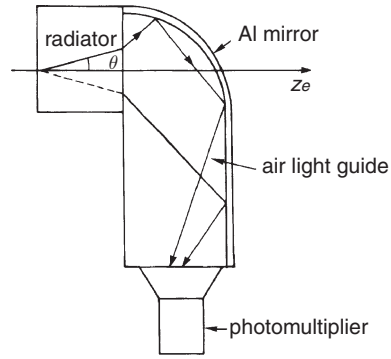


Fig. 5.41. Working principle of a differential (Fitch-type) Cherenkov counter [149–151].

escape into the air light guide. The critical angle for internal reflection can be computed from Snell's law of refraction to be

$$\sin\theta_{\mathrm{t}} = \frac{1}{n} \ . \tag{5.82}$$

Because

$$\cos\theta = \sqrt{1-\sin^2\theta} = \frac{1}{n\beta} \tag{5.83}$$

the maximum detectable velocity is

$$\beta_{\max} = \frac{1}{\sqrt{n^2-1}} \ . \tag{5.84}$$

For polystyrene ($n = 1.6$) $\beta_{\min}$ is 0.625 and $\beta_{\max}$ is equal to 0.80. In this way, such a differential Cherenkov counter selects a velocity window of about $\Delta\beta = 0.17$. If the optical system of a differential Cherenkov counter is optimised, so that chromatic aberrations are corrected (DISC counter, DIScriminating Cherenkov counter [152]), a velocity resolution of $\Delta\beta/\beta = 10^{-7}$ can be achieved. The main types of Cherenkov detectors are discussed in Chap. 9.

## 5.7 Transition-radiation detectors (TRD)

Below Cherenkov threshold, charged particles can also emit electromagnetic radiation. This radiation is emitted in those cases where charged particles traverse the boundary between media with different dielectric properties [153]. This occurs, for example, when a charged particle enters a dielectric through a boundary from the vacuum or from air, respectively.

https://doi.org/10.1017/9781009401531.008 Published online by Cambridge University Press

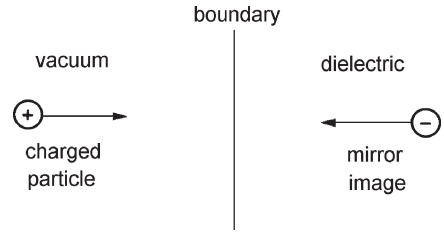


Fig. 5.42. Illustration of the production of transition radiation at boundaries.

The energy loss by *transition radiation* represents only a negligibly small contribution to the total energy loss of charged particles.

A charged particle moving towards a boundary forms together with its mirror charge an electric dipole, whose field strength varies in time, i.e. with the movement of the particle (Fig. 5.42). The field strength vanishes when the particle enters the medium. The time-dependent dipole electric field causes the emission of electromagnetic radiation.

The emission at boundaries can be understood in such a way that although the electric displacement $\vec{D} = \varepsilon\varepsilon_0\vec{E}$ varies continuously in passing through the boundary, the electric field strength does not [154–156].

The energy radiated from a single boundary (transition from vacuum to a medium with dielectric constant $\varepsilon$) is proportional to the Lorentz factor of the incident charged particle [157–159]:

$$S = \frac{1}{3}\alpha z^2 \hbar\omega_\mathrm{p}\gamma \ , \ \ \hbar\omega_\mathrm{p} = \sqrt{4\pi N_e r_e^3} m_e c^2/\alpha \ , \tag{5.85}$$

where $N_e$ is the electron density in the material, $r_e$ is classical electron radius, and $\hbar\omega_\mathrm{p}$ is the *plasma energy*. For commonly used plastic radiators (styrene or similar materials) one has

$$\hbar\omega_\mathrm{p} \approx 20\,\mathrm{eV} \ . \tag{5.86}$$

The radiation yield drops sharply for frequencies

$$\omega > \gamma\omega_\mathrm{p} \ . \tag{5.87}$$

The number of emitted transition-radiation photons with energy $\hbar\omega$ higher than a certain threshold $\hbar\omega_0$ is

$$N_\gamma(\hbar\omega > \hbar\omega_0) \approx \frac{\alpha z^2}{\pi}\left[\left(\ln\frac{\gamma\hbar\omega_\mathrm{p}}{\hbar\omega_0} - 1\right)^2 + \frac{\pi^2}{12}\right] \ . \tag{5.88}$$

https://doi.org/10.1017/9781009401531.008 Published online by Cambridge University Press

At each interface the emission probability for an X-ray photon is on the order of $\alpha = 1/137$.

The number of transition-radiation photons produced can be increased if the charged particle traverses a large number of boundaries, e.g. in porous media or periodic arrangements of foils and air gaps.

The attractive feature of transition radiation is that the energy radiated by transition-radiation photons increases with the Lorentz factor $\gamma$ (i.e. the energy) of the particle, and is not proportional only to its velocity [160, 161]. Since most processes used for particle identification (energy loss by ionisation, time of flight, Cherenkov radiation, etc.) depend on the velocity, thereby representing only very moderate identification possibilities for relativistic particles ($\beta \to 1$), the $\gamma$-dependent effect of transition radiation is extremely valuable for particle identification at high energies.

An additional advantage is the fact that transition-radiation photons are emitted in the X-ray range [162]. The increase of the radiated energy in transition radiation proportional to the Lorentz factor originates mainly from the increase of the average energy of X-ray photons and much less from the increase of the radiation intensity. In Fig. 5.43 the average energy of transition-radiation photons is shown in its dependence on the electron momentum for a typical radiator [152].

The angle of emission of transition-radiation photons is inversely proportional to the Lorentz factor,

$$\theta = \frac{1}{\gamma_{\text{particle}}} \ . \tag{5.89}$$

For periodical arrangements of foils and gaps, interference effects occur, which produce an effective threshold behaviour at a value of $\gamma \approx 1000$

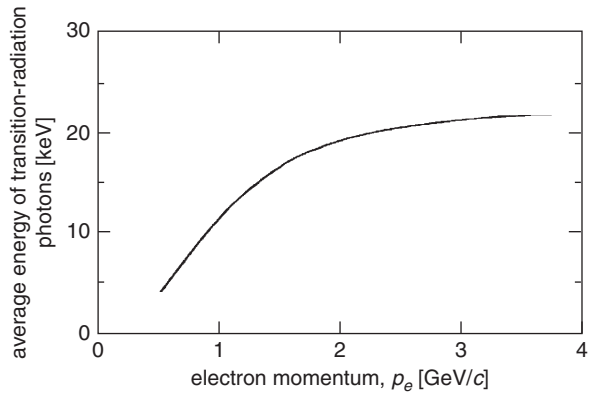


Fig. 5.43. Typical dependence of the average energy of transition-radiation photons on the electron momentum for standard-radiator arrangements [152].

https://doi.org/10.1017/9781009401531.008 Published online by Cambridge University Press

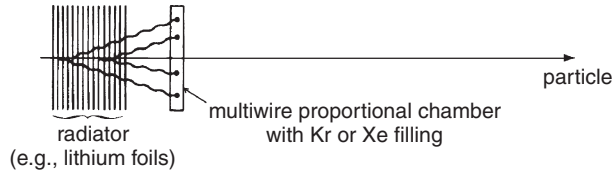


Fig. 5.44. Working principle of a transition-radiation detector.

[163, 164], i.e., for particles with $\gamma < 1000$ almost no transition-radiation photons are emitted.

A typical arrangement of a *transition-radiation detector* (TRD) is shown in Fig. 5.44. The TRD is formed by a set of foils consisting of a material with an atomic number $Z$ as low as possible. Because of the strong dependence of the photoabsorption cross section on $Z(\sigma_{\text{photo}} \propto Z^5)$ the transition-radiation photons would otherwise not be able to escape from the radiator. The transition-radiation photons have to be recorded in a detector with a high efficiency for X-ray photons. This requirement is fulfilled by a multiwire proportional chamber filled with krypton or xenon, i.e. gases with high atomic number for an effective absorption of X rays.

In the set-up sketched in Fig. 5.44 the charged particle also traverses the photon detector, leading to an additional energy deposit by ionisation and excitation. This energy loss is superimposed onto the energy deposit by transition radiation. Figure 5.45 shows the energy-loss distribution in a transition-radiation detector for highly relativistic electrons for the case that (a) the radiator has gaps and (b) the radiator has no gaps (dummy). In both cases the amount of material in the radiators is the same. In the first case, because of the gaps, transition-radiation photons are emitted,

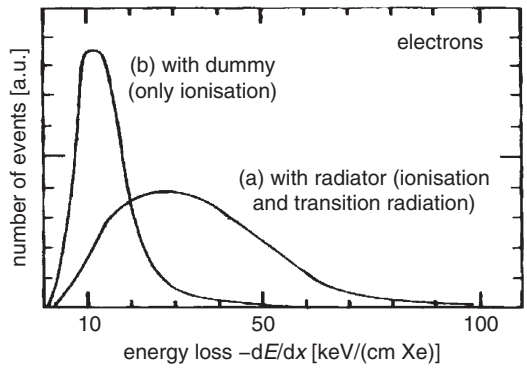


Fig. 5.45. Typical energy-loss distribution for high-energy electrons in a transition-radiation detector with radiator and with dummy radiator [152].

https://doi.org/10.1017/9781009401531.008 Published online by Cambridge University Press

leading to an increased average energy loss of electrons, while in the second case only the ionisation loss of electrons is measured [152].

## 5.8 Problems

**5.1** A Geiger–Müller counter (dead time 500 µs) measures in a strong radiation field a count rate of 1 kHz. What is the dead-time corrected true rate?

**5.2** In practical situations the energy measurement in a semiconductor counter is affected by some dead layer of thickness $d$, which is usually unknown, in front of the sensitive volume. How can $d$ be determined experimentally?

**5.3** The Cherenkov angle is normally derived to be related to the particle velocity $\beta$ and index of refraction $n$ according to

$$\cos \Theta = \frac{1}{n\beta} \ .$$

This, however, neglects the recoil of the emitted Cherenkov photon on the incident particle. Determine the exact relation for the Cherenkov angle considering the recoil effect.

**5.4** A detector may consist of a spherical vessel of radius $R$ filled with liquid scintillator which is read out by a photomultiplier tube with photocathode area $S_\mathrm{p} \ll S_\mathrm{tot} = 4\pi R^2$ (Fig. 5.46). All inner surface of the vessel except the output window is covered with a diffusive

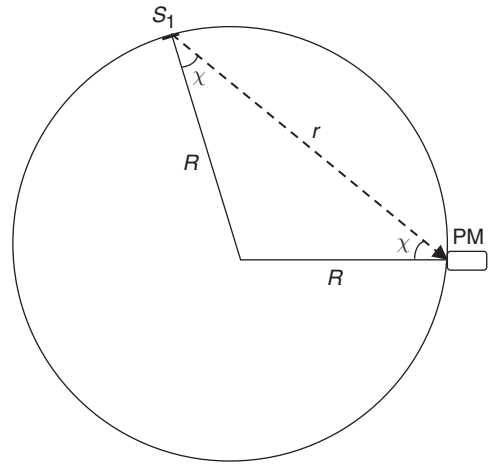


Fig. 5.46. Illustration for Problem 5.4.

https://doi.org/10.1017/9781009401531.008 Published online by Cambridge University Press

reflector of efficiency $(1-\mu)$. Estimate the light collection efficiency if the diffusive reflection is governed by Lambert's law [165]: $\mathrm{d}J = (J_0/\pi)\cdot\cos\chi\cdot\mathrm{d}\Omega$, where $J_0$ is the total amount of the reflected light and $\chi$ is the angle between the observation line and the normal to the surface. The detector is irradiated uniformly.

## References


[1] Particle Data Group, Review of Particle Physics, S. Eidelman *et al.*, *Phys. Lett.* **B592 Vol. 1–4** (2004) 1–1109; W.-M. Yao *et al.*, *J. Phys.* **G33** (2006) 1–1232; http://pdg.lbl.gov

[2] B. Rossi & H. Staub, *Ionization Chambers and Counters*, McGraw-Hill, New York (1949)

[3] D.M. Wilkinson, *Ionization Chambers and Counters*, Cambridge University Press, Cambridge (1950)

[4] O.C. Allkofer, *Teilchendetektoren*, Thiemig, München (1971)

[5] O.R. Frisch, *British Atomic Energy Report* **BR-49** (1944)

[6] R. Feynman, *The Feynman Lectures on Physics*, Vol. 2, Addison-Wesley, Reading, MA (1964)

[7] D. McCormick, *Fast Ion Chambers for SLC*, SLAC-Pub-6296 (1993)

[8] M. Fishman & D. Reagan, The SLAC Long Ion Chamber For Machine Protection, *IEEE Trans. Nucl. Sci.* **NS-14** (1967) 1096–8

[9] E. Sauter, *Grundlagen des Strahlenschutzes*, Siemens AG, Berlin/ München (1971); *Grundlagen des Strahlenschutzes*, Thiemig, München (1982)

[10] S.E. Hunt, *Nuclear Physics for Engineers and Scientists*, John Wiley & Sons Inc. (Wiley Interscience), New York (1987)

[11] J.S. Townsend, *Electricity in Gases*, Clarendon Press, Oxford (1915)

[12] S.C. Brown, *Introduction to Electrical Discharges in Gases*, John Wiley & Sons Inc. (Wiley Interscience), New York (1966)

[13] H. Raether, *Electron Avalanches and Breakdown in Gases*, Butterworth, London (1964)

[14] A. Sharma & F. Sauli, A Measurement of the First Townsend Coefficient in Ar-based Mixtures at High Fields, *Nucl. Instr. Meth.* **A323** (1992) 280–3

[15] A. Sharma & F. Sauli, First Townsend Coefficient Measured in Argon Based Mixtures at High Fields, *Nucl. Instr. Meth.* **A334** (1993) 420–4

[16] F. Sauli, *Principles of Operation of Multiwire Proportional and Drift Chambers*, CERN-77-09 (1977) and references therein

[17] S.C. Brown, *Basic Data of Plasma Physics*, MIT Press, Cambridge, MA (1959), and John Wiley & Sons Inc., New York (1959)

[18] A. von Engel, Ionization in Gases by Electrons in Electric Fields, in S. Flügge (ed.), *Handbuch der Physik*, Elektronen-Emission; Gasentladungen I, Bd. **XXI**, Springer, Berlin (1956)

[19] A. Arefev *et al.*, *A Measurement of the First Townsend Coefficient in $CF_4$, $CO_2$, and $CF_4/CO_2$-Mixtures at High, Uniform Electric Field*, RD5 Collaboration, CERN-PPE-93-082 (1993)

[20] E. Bagge & O.C. Allkofer, Das Ansprechvermögen von Parallel-Platten Funkenzählern für schwach ionisierende Teilchen, *Atomenergie* **2** (1957) 1–17

[21] B. Sitar, G.I. Merson, V.A. Chechin & Yu.A. Budagov, *Ionization Measurements in High Energy Physics* (in Russian), Energoatomizdat, Moskau (1988)

[22] B. Sitar, G.I. Merson, V.A. Chechin & Yu.A. Budagov, *Ionization Measurements in High Energy Physics*, Springer Tracts in Modern Physics, Vol. 124, Springer, Berlin/Heidelberg (1993)

[23] L.G. Huxley & R.W. Crompton, *The Diffusion and Drift of Electrons in Gases*, John Wiley & Sons Inc. (Wiley Interscience), New York (1974)

[24] T.Z. Kowalski, Generalised Parametrization of the Gas Gain in Proportional Counters, *Nucl. Instr. Meth.* **A243** (1986) 501–4; On the Generalised Gas Gain Formula for Proportional Counters, *Nucl. Instr. Meth.* **A244** (1986) 533–6; Measurement and Parametrization of the Gas Gain in Proportional Counters, *Nucl. Instr. Meth.* **A234** (1985) 521–4

[25] T. Aoyama, Generalised Gas Gain Formula for Proportional Counters, *Nucl. Instr. Meth.* **A234** (1985) 125–31

[26] H.E. Rose & S.A. Korff, Investigation of Properties of Proportional Counters, *Phys. Rev.* **59** (1941) 850–9

[27] A. Williams & R.I. Sara, Parameters Effecting the Resolution of a Proportional Counter, *Int. J. Appl. Radiation Isotopes* **13** (1962) 229–38

[28] M.W. Charles, Gas Gain Measurements in Proportional Counters, *J. Phys.* **E5** (1972) 95–100

[29] A. Zastawny, Gas Amplification in a Proportional Counter with Carbon Dioxide, *J. Sci. Instr.* **43** (1966) 179–81; *Nukleonika* **11** (1966) 685–90

[30] L.G. Kristov, Measurement of the Gas Gain in Proportional Counters, *Doklady Bulg. Acad. Sci.* **10** (1947) 453–7

[31] L.B. Loeb, *Basis Processes of Gaseous Electronics*, University of California Press, Berkeley (1961)

[32] G.A. Schröder, Discharge in Plasma Physics, in S.C. Haydon (ed.), *Summer School Univ. of New England*, The University of New England, Armidale (1964)

[33] M. Salehi, *Nuklididentifizierung durch Halbleiterspektrometer*, Diploma Thesis, University of Siegen (1990)

[34] V. Aulchenko *et al.*, Fast, parallax-free, one-coordinate X-ray detector OD-3, *Nucl. Instr. Meth.* **A405** (1998) 269–73

[35] G.C. Smith *et al.*, High Rate, High Resolution, Two-Dimensional Gas Proportional Detectors for X-Ray Synchrotron Radiation Experiments, *Nucl. Instr. Meth.* **A323** (1992) 78–85

[36] G. Charpak, *Electronic Imaging of Ionizing Radiation with Limited Avalanches in Gases*, Nobel-Lecture 1992, CERN-PPE-93-25 (1993); *Rev. Mod. Phys.* **65** (1993) 591–8

[37] H. Geiger, Method of Counting $\alpha$ and $\beta$-Rays, *Verh. d. Deutsch. Phys. Ges.* **15** (1913) 534–9

[38] E. Rutherford & H. Geiger, An Electrical Method of Counting the Number of $\alpha$-Particles from Radio-active Substances, *Proc. R. Soc. Lond.* **81** (1908) 141–61

[39] H. Geiger & W. Müller, Das Elektronenzählrohr, *Z. Phys.* **29** (1928) 839–41; Technische Bemerkungen zum Elektronenzählrohr, *Z. Phys.* **30** (1929) 489–93

[40] G.D. Alekseev, D.B. Khazins & V.V. Kruglov, Selfquenching Streamer Discharge in a Wire Chamber, *Lett. Nuovo Cim.* **25** (1979) 157–60; *Fiz. Elem. Chast. Atom. Yadra* **13** (1982) 703–48; Investigation of Selfquenching Streamer Discharge in a Wire Chamber, *Nucl. Instr. Meth.* **177** (1980) 385–97

[41] E. Iarocci, Plastic Streamer Tubes and Their Applications in High Energy Physics, *Nucl. Instr. Meth.* **217** (1983) 30–42

[42] G. Battistoni *et al.*, Operation of Limited Streamer Tubes, *Nucl. Instr. Meth.* **164** (1979) 57–66

[43] G.D. Alekseev, Investigation of Self-Quenching Streamer Discharge in a Wire Chamber, *Nucl. Instr. Meth.* **177** (1980) 385–97

[44] R. Baumgart *et al.*, The Response of a Streamer Tube Sampling Calorimeter to Electrons, *Nucl. Instr. Meth.* **A239** (1985) 513–17; Performance Characteristics of an Electromagnetic Streamer Tube Calorimeter, *Nucl. Instr. Meth.* **A256** (1987) 254–60; Interactions of 200 GeV Muons in an Electromagnetic Streamer Tube Calorimeter, *Nucl. Instr. Meth.* **A258** (1987) 51–7; Test of an Iron/Streamer Tube Calorimeter with Electrons and Pions of Energy between 1 and 100 GeV, *Nucl. Instr. Meth.* **A268** (1988) 105–11

[45] R. Baumgart *et al.*, Properties of Streamers in Streamer Tubes, *Nucl. Instr. Meth.* **222** (1984) 448–57

[46] *Dubna: Self Quenching Streamers Revisited*, CERN-Courier, **21(8)** (1981) 358

[47] T. Doke, A Historical View on the R&D for Liquid Rare Gas Detectors, *Nucl. Instr. Meth.* **A327** (1993) 113–18

[48] T. Doke (ed.), Liquid Radiation Detectors, *Nucl. Instr. Meth.* **A327** (1993) 3–226

[49] T.S. Virdee, Calorimeters Using Room Temperature and Noble Liquids, *Nucl. Instr. Meth.* **A323** (1992) 22–33

[50] A.A. Grebenuk, Liquid Noble Gas Calorimeters for KEDR and CMD-2M Detectors, *Nucl. Instr. Meth.* **A453** (2000) 199–204

[51] M. Jeitler, The NA48 Liquid-Krypton Calorimeter, *Nucl. Instr. Meth.* **A494** (2002) 373–7

[52] C. Ramsauer & R. Kollath, Die Winkelverteilung bei der Streuung langsamer Elektronen an Gasmolekülen, *Ann. Phys.* **401** (1931) 756–68

[53] C. Ramsauer & R. Kollath, Über den Wirkungsquerschnitt der Edelgasmoleküle gegenüber Elektronen unterhalb 1 Volt, *Ann. Phys.* **395** (1929) 536–64

[54] C. Ramsauer, Über den Wirkungsquerschnitt der Gasmoleküle gegenüber langsamen Elektronen, *Ann. Phys.* **64** (1921) 513–40

[55] E. Brüche *et al.*, Über den Wirkungsquerschnitt der Edelgase Ar, Ne, He gegenüber langsamen Elektronen, *Ann. Phys.* **389** (1927) 279–91

[56] C.E. Normand, The Absorption Coefficient for Slow Electrons in Gases, *Phys. Rev.* **35** (1930) 1217–25

[57] D. Acosta *et al.*, Advances in Technology for High Energy Subnuclear Physics. Contribution of the LAA Project, *Riv. del Nuovo Cim.* **13(10–11)** (1990) 1–228; and G. Anzivino *et al.*, The LAA Project, *Riv. del Nuovo Cim.* **13(5)** (1990) 1–131

[58] J. Engler, H. Keim & B. Wild, Performance Test of a TMS Calorimeter, *Nucl. Instr. Meth.* **A252** (1986) 29–34

[59] M.G. Albrow *et al.*, Performance of a Uranium/Tetramethylpentane Electromagnetic Calorimeter, *Nucl. Instr. Meth.* **A265** (1988) 303–18

[60] K. Ankowiak *et al.*, Construction and Performance of a Position Detector for the UA1 Uranium-TMP Calorimeter, *Nucl. Instr. Meth.* **A279** (1989) 83–90

[61] M. Pripstein, *Developments in Warm Liquid Calorimetry*, LBL-30282, Lawrence-Berkeley Laboratory (1991); B. Aubert *et al.*, *Warm Liquid Calorimetry*, Proc. 25th Int. Conf. on High Energy Physics, Singapore, Vol. 2 (1991) 1368–71; B. Aubert *et al.*, A Search for Materials Compatible with Warm Liquids, *Nucl. Instr. Meth.* **A316** (1992) 165–73

[62] J. Engler, Liquid Ionization Chambers at Room Temperatures, *J. Phys. G: Nucl. Part. Phys.* **22** (1996) 1–23

[63] G. Bressi *et al.*, Electron Multiplication in Liquid Argon on a Tip Array, *Nucl. Instr. Meth.* **A310** (1991) 613–7

[64] R.A. Muller *et al.*, Liquid Filled Proportional Counter, *Phys. Rev. Lett.* **27** (1971) 532–6

[65] S.E. Derenzo *et al.*, *Liquid Xenon-Filled Wire Chambers for Medical Imaging Applications*, LBL-2092, Lawrence-Berkeley Laboratory (1973)

[66] E. Aprile, K.L. Giboni & C. Rubbia, *A Study of Ionization Electrons Drifting Large Distances in Liquid and Solid Argon*, Harvard University Preprint (May 1985)

[67] C. Kittel, *Introduction to Solid State Physics*, 8th edition, Wiley Interscience, New York (2005), and *Einführung in die Festkörperphysik*, Oldenbourg, München/Wien (1980)

[68] G.F. Knoll, *Radiation Detection and Measurement*, 3rd edition, John Wiley & Sons Inc., New York (Wiley Interscience), New York (1999/2000)

[69] S.M. Sze, *Physics of semiconductor devices*, 2nd edition, Wiley, New York (1981)

[70] P. Sangsingkeow *et al.*, Advances in Germanium Detector Technology, *Nucl. Instr. Meth.* **A505** (2003) 183–6

[71] G. Bertolini & A. Coche (eds.), *Semiconductor Detectors*, Elsevier–North Holland, Amsterdam (1968)

[72] V. Zhilich, private communication

[73] S.P. Beaumont *et al.*, Gallium Arsenide Microstrip Detectors for Charged Particles, *Nucl. Instr. Meth.* **A321** (1992) 172–9

[74] A.I. Ayzenshtat *et al.*, GaAs as a Material for Particle Detectors, *Nucl. Instr. Meth.* **A494** (2002) 120–7

[75] R.H. Redus *et al.*, Multielement CdTe Stack Detectors for Gamma-Ray Spectroscopy, *IEEE Trans. Nucl. Sci.* **51(5)** (2004) 2386–94

[76] A.H. Walenta, Strahlungsdetektoren – Neuere Entwicklungen und Anwendungen, *Phys. Bl.* **45** (1989) 352–6

[77] R. Kelley, D. McCammon *et al.*, *High Resolution X-Ray Spectroscopy Using Microcalorimeters*, NASA-Preprint LHEA 88-026 (1988); publ. in 'X-Ray Instrumentation in Astronomy', Proc. S.P.I.E. 982 (1988) 219–24; D. McCammon *et al.*, Cryogenic microcalorimeters for high resolution spectroscopy: Current status and future prospects, *Nucl. Phys.* **A527** (1991) 821C–4C

[78] F. Cardone & F. Celani, Rivelatori a Bassa Temperatura e Superconduttori per la Fisica delle Particelle di Bassa Energia, *Il Nuovo Saggiatore* **6(3)** (1990) 51–61

[79] A. Matsumura *et al.*, High Resolution Detection of X-Rays with a Large Area Nb/Al – Al $O_x$/Al/Nb Superconducting Tunnel Injection, *Nucl. Instr. Meth.* **A309** (1991) 350–2

[80] G. Hertz, *Lehrbuch der Kernphysik*, Bd. 1, Teubner, Leipzig (1966)

[81] J. Chadwick, Observations Concerning Artificial Disintegration of Elements, *Phil. Mag.* **7(2)** (1926) 1056–61

[82] V. Henri & J. Larguier des Bancels, Photochimie de la Rétine, *Journ. de Physiol. et de Pathol. Gén.* **XIII** (1911) 841–58; Anwendung der physikalisch-chemischen Untersuchungsmethoden auf das Studium verschiedener allgemein-biologischer Erscheinungen *Journ. de Physiol. et de Pathol. Gén.* **2** (Mars 1904)

[83] D.A. Baylor, Photoreceptor Signals and Vision: Proctor Lecture. *Investigative Ophthalmology and Visual Science*, **28** (1987) 34–49

[84] K.W.F. Kohlrausch, Radioaktivität, in W. Wien & F. Harms (eds.), *Handbuch der Experimentalphysik*, Band **15**, Akademische Verlagsanstalt, Leipzig (1928)

[85] R. Hofstadter, Alkali Halide Scintillation Counters, *Phys. Rev.* **74** (1948) 100–1; and Erratum: Alkali Halide Scintillation Counters, *Phys. Rev.* **74** (1948) 628

[86] R. Hofstadter & J.A. McIntyre, Gamma-Ray Spectroscopy with Crystals of NaI(Tl), *Nucleonics* **7** (1950) 32–7

[87] J.B. Birks, *The Theory and Practice of Scintillation Counting*, Pergamon Press, Oxford (1964, 1967); *Scintillation Counters*, Pergamon Press, Oxford (1953)

[88] K.D. Hildenbrand, *Scintillation Detectors*, Darmstadt GSI-Preprint GSI 93-18 (1993)

[89] E.B. Norman, *Scintillation Detectors*, LBL-31371, Lawrence-Berkeley Laboratory (1991)

[90] R. Hofstadter, *Twenty-Five Years of Scintillation Counting*, IEEE Scintillation and Semiconductor Counter Symposium, Washington DC, HEPL Report No. 749, Stanford University (1974)
[91] R. Novotny, Inorganic Scintillators: A Basic Material for Instrumentation in Physics, *Nucl. Instr. Meth.* **A537** (2005) 1–5
[92] C. Amsler *et al.*, Temperature Dependence of Pure CsI: Scintillation Light Yield and Decay Time, *Nucl. Instr. Meth.* **A480** (2002) 494–500
[93] Scintillation materials & Detectors, Catalogue of Amcrys-H, Kharkov, Ukraine (2000)
[94] Scintillation Detectors, Crismatec, Catalogue (1992)
[95] I. Holl, E. Lorenz & G. Mageras, A Measurement of the Light Yield of Some Common Inorganic Scintillators, *IEEE Trans. Nucl. Sci.* **35(1)** (1988) 105–9
[96] C.L. Melcher & J.S. Schweitzer, A Promising New Scintillator: Cerium-doped Luthetium Oxyorthosilicate, *Nucl. Instr. Meth.* **A314** (1992) 212–14
[97] M. Moszynski *et al.*, Large Size LSO:Ce and YSO:Ce Scintillators for 50 MeV Range $\gamma$-ray Detector, *IEEE Trans. Nucl. Sci.* **47**, No. 4 (2000) 1324–8
[98] M.E. Globus & B.V. Grinyov, Inorganic Scintillation Crystals: New and Traditional Materials, Kharkov (Ukraine), Akta (2000)
[99] C.L. Melcher, Perspectives on the Future Development of New Scintillators, *Nucl. Instr. Meth.* **A537** (2005) 6–14
[100] T. Förster, Zwischenmolekulare Energiewanderung und Fluoreszenz, *Ann. Phys.* **2** (1948) 55–67
[101] K. Kleinknecht, *Detektoren für Teilchenstrahlung*, Teubner, Stuttgart (1984, 1987, 1992); *Detectors for Particle Radiation*, Cambridge University Press, Cambridge (1986)
[102] Saint-Gobain, Crystals and Detectors, Organic Scintillators; General Characteristics and Technical Data; www.detectors.saint-gobain.com
[103] 'Physical Properties of Plastic Scintillators', www.amcrys-h.com/plastics.htm, www.amcrys-h.com/organics.htm
[104] R.B. Murray & A. Meyer, Scintillation Response of Activated Inorganic Crystals to Various Charged Particles, *Phys. Rev.* **122** (1961) 815–26
[105] W. Mengesha *et al.*, Light Yield Nonproportionality of CsI(Tl), CsI(Na) and YAP, *IEEE Trans. Nucl. Sci.* **45(3)** (1998) 456–60
[106] B.A. Dolgoshein & B.U. Rodionov, The Mechanism of Noble Gas Scintillation, *Elementary Particles and Cosmic Rays*, No. 2, Sect. 6.3, Atomizdat, Moscow (1969)
[107] T. Doke & K. Masuda, Present Status of Liquid Rare Gas Scintillation Detectors and Their New Application to Gamma-ray Calorimetry, *Nucl. Instr. Meth.* **A420** (1999) 62–80
[108] B. Mouellic, *A Comparative Study of the Reflectivity of Several Materials Used for the Wrapping of Scintillators in Particle Physics Experiments*, CERN-PPE-94-194, CERN (1994)

[109] B.J. Pichler *et al.*, Production of a Diffuse Very High Reflectivity Material for Light Collection in Nuclear Detectors, *Nucl. Instr. Meth.* **A442** (2000) 333–6
[110] Nuclear Enterprises, *Scintillation Materials*, Edinburgh (1977)
[111] Photomultiplier Tubes: Principles & Applications, Re-edited by S.-O. Flyct & C. Marmonier, Photonis, Brive, France (2002)
[112] Hamamatsu Photonics K.K., Editorial Committee, *Photomultipliers Tubes, Basics and Applications*, 2nd edition, Hamamatsu (1999)
[113] *Si Photodiode*, Catalogue, Hamamatsu Photonics K.K., Solid State Division, Hamamatsu (2002)
[114] Photomultiplier tubes, Catalogue Photonis, Brive, France (2000)
[115] K.S. Hirata *et al.*, Observation of a Neutrino Burst from the Supernova SN 1987 A, *Phys. Rev. Lett.* **58** (1987) 1490–3
[116] K.S. Hirata *et al.*, *Observation of $^8B$ Solar Neutrinos in the Kamiokande II Detector*, Inst. f. Cosmic Ray Research, ICR-Report 188-89-5 (1989)
[117] Hamamatsu Photonics K.K., *Measure Weak Light from Indeterminate Sources with New Hemispherical PM*, CERN-Courier, **21(4)** (1981) 173; private communication by Dr. H. Reiner, Hamamatsu Photonics, Germany
[118] K. Blazek *et al.*, YAP Multi-Crystal Gamma Camera Prototype, *IEEE Trans. Nucl. Sci.* **42(5)** (1995) 1474–82
[119] J. Bibby *et al.*, Performance of Multi-anode Photomultiplier Tubes for the LHCb RICH detectors, *Nucl. Instr. Meth.* **A546** (2005) 93–8
[120] E. Aguilo *et al.*, Test of Multi-anode Photomultiplier Tubes for the LHCb Scintillator Pad Detector, *Nucl. Instr. Meth.* **A538** (2005) 255–64
[121] Philips, *Imaging: From X-Ray to IR*, CERN-Courier, **23(1)** (1983) 35
[122] M. Akatsu *et al.*, MCP-PMT Timing Property for Single Photons, *Nucl. Instr. Meth.* **A528** (2004) 763–75
[123] G. Anzivino *et al.*, Review of the Hybrid Photo Diode Tube (HPD) an Advanced Light Detector for Physics, *Nucl. Instr. Meth.* **A365** (1995) 76–82
[124] C. D'Ambrosio & H. Leutz, Hybrid Photon Detectors, *Nucl. Instr. Meth.* **A501** (2003) 463–98
[125] C. D'Ambrosio *et al.*, Gamma Spectroscopy and Optoelectronic Imaging with Hybrid Photon Detector, *Nucl. Instr. Meth.* **A494** (2003) 186–97
[126] D.N. Grigoriev *et al.*, Study of a Calorimeter Element Consisting of a Csi(Na) Crystal and a Phototriode, *Nucl. Instr. Meth.* **A378** (1996) 353–5
[127] P.M. Beschastnov *et al.*, The Results of Vacuum Phototriodes Tests, *Nucl. Instr. Meth.* **A342** (1994) 477–82
[128] P. Checchia *et al.*, Study of a Lead Glass Calorimeter with Vacuum Phototriode Readout, *Nucl. Instr. Meth.* **A248** (1986) 317–25
[129] H. Grassman, E. Lorenz, H.G. Mozer & H. Vogel, Results from a CsI(Tl) Test Calorimeter with Photodiode Readout between 1 GeV and 20 GeV, *Nucl. Instr. Meth.* **A235** (1985) 319–25
[130] H. Dietl *et al.*, Reformance of BGO Calorimeter with Photodiode Readout and with Photomultiplier Readout at Energies up to 10 GeV, *Nucl. Instr. Meth.* **A235** (1985) 464–74

[131] S.J. Fagen (ed.), *The Avalanche Photodiode Catalog*, Advanced Photonix Inc., Camarillo, CA93012, USA (1992)

[132] E. Lorenz *et al.*, *Test of a Fast, Low Noise Readout of Pure CsI Crystals with Avalanche Photodiodes*, Proc. 4th Int. Conf. on Calorimetry in High-energy Physics, La Biodola, Italy (19–25 September 1993) 102–6

[133] E. Lorenz *et al.*, Fast Readout of Plastic and Crystal Scintillators by Avalanche Photodiodes, *Nucl. Instr. Meth.* **A344** (1994) 64–72

[134] I. Britvich *et al.*, Avalanche Photodiodes Now and Possible Developments, *Nucl. Instr. Meth.* **A535** (2004) 523–7

[135] R.J. McIntyre, Multiplication Noise in Uniform Avalanche Diodes, *IEEE Trans. on Electron Devices* **ED-13** (1966) 164–8

[136] P.P. Webb, R.J. McIntyre & J. Conradi, Properties of Avalanche Photodiodes, *RCA Review* **35** (1974) 234–78

[137] A.N. Otte *et al.*, A Test of Silicon Photomultipliers as Readout for PET, *Nucl. Instr. Meth.* **A545** (2005) 705–15

[138] P.A. Cherenkov, Visible Radiation Produced by Electrons Moving in a Medium with Velocities Exceeding that of Light, *Phys. Rev.* **52** (1937) 378–9

[139] P.A. Cherenkov, *Radiation of Particles Moving at a Velocity Exceeding that of Light, and some of the Possibilities for Their Use in Experimental Physics*, and I.M. Frank, *Optics of Light Sources Moving in Refractive Media*, and I.E. Tamm, *General Characteristics of Radiations Emitted by Systems Moving with Super Light Velocities with some Applications to Plasma Physics*, Nobel Lectures 11 December, 1958, publ. in *Nobel Lectures in Physics 1942–62*, Elsevier Publ. Comp., New York (1964) 426–40 (Cherenkov), 471–82 (Tamm) and 443–68 (Frank)

[140] P. Marmier & E. Sheldon, *Physics of Nuclei and Particles*, Vol. 1, Academic Press, New York (1969)

[141] J.V. Jelley, *Cherenkov Radiation and its Applications*, Pergamon Press, London/New York (1958)

[142] C. Grupen & E. Hell, Lecture Notes, *Kernphysik*, University of Siegen (1983)

[143] R.C. Weast & M.J. Astle (eds.), *Handbook of Chemistry and Physics*, CRC Press, Boca Raton, Florida (1979, 1987)

[144] M. Born & E. Wolf, *Principles of Optics*, Pergamon Press, New York (1964)

[145] N.W. Ashcroft & N.D. Mermin, *Solid State Physics*, Holt-Saunders, New York (1976)

[146] A.F. Danilyuk *et al.*, Recent Results on Aerogel Development for Use in Cherenkov Counters, *Nucl. Instr. Meth.* **A494** (2002) 491–4

[147] G. Poelz & R. Reithmuller, Preparation of Silica Aerogel for Cherenkov Counters, *Nucl. Instr. Meth.* **195** (1982) 491–503

[148] E. Nappi, Aerogel and its Applications to RICH Detectors, ICFA Instrumentation Bulletin and SLAC-JOURNAL-ICFA-17-3, *Nucl. Phys. B Proc. Suppl.* **61** (1998) 270–6

[149] H. Bradner & D.A. Glaser, *Methods of Particle Identification for High energy Physics Experiments*, 2nd United Nations International Conference on Peaceful Uses of Atomic Energy, A/CONF.15/P/730/Rev. 1 (1958)
[150] C. Biino *et al.*, A Glass Spherical Cherenkov Counter Based on Total Internal Reflection, *Nucl. Instr. Meth.* **A295** (1990) 102–8
[151] V. Fitch & R. Motley, Mean Life of $K^+$ Mesons, *Phys. Rev.* **101** (1956) 496–8; Lifetime of $\tau^+$ Mesons, *Phys. Rev.* **105** (1957) 265–6
[152] C.W. Fabjan & H.G. Fischer, *Particle Detectors*, CERN-EP-80-27 (1980)
[153] V.L. Ginzburg & V.N. Tsytovich, *Transition Radiation and Transition Scattering*, Inst. of Physics Publishing, Bristol (1990)
[154] A. Bodek *et al.*, Observation of Light Below Cherenkov Threshold in a 1.5 Meter Long Integrating Cherenkov Counter, *Z. Phys.* **C18** (1983) 289–306
[155] W.W.M. Allison & J.H. Cobb, Relativistic Charged Particle Identification by Energy Loss, *Ann. Rev. Nucl. Sci.* **30** (1980) 253–98
[156] W.W.M. Allison & P.R.S. Wright, *The Physics of Charged Particle Identification:* $\mathrm{d}E/\mathrm{d}x$*, Cherenkov and Transition Radiation*, Oxford University Preprint OUNP 83-35 (1983)
[157] Particle Data Group, R.M. Barnett *et al.*, *Phys. Rev.* **D54** (1996) 1–708; *Eur. Phys. J.* **C3** (1998) 1–794; *Eur. Phys. J.* **C15** (2000) 1–878
[158] R.C. Fernow, *Brookhaven Nat. Lab. Preprint* **BNL-42114** (1988)
[159] S. Paul, *Particle Identification Using Transition Radiation Detectors*, CERN-PPE-91-199 (1991)
[160] B. Dolgoshein, Transition Radiation Detectors, *Nucl. Instr. Meth.* **A326** (1993) 434–69
[161] V.L. Ginzburg & I.M. Frank, Radiation of a Uniformly Moving Electron due to its Transitions from One Medium into Another, *JETP* **16** (1946) 15–29
[162] G.M. Garibian, *Macroscopic Theory of Transition Radiation*, Proc. 5th Int. Conf. on Instrumentation for High Energy Physics, Frascati (1973) 329–33
[163] X. Artru *et al.*, Practical Theory of the Multilayered Transition Radiation Detector, *Phys. Rev.* **D12** (1975) 1289–306
[164] J. Fischer *et al.*, Lithium Transition Radiator and Xenon Detector Systems for Particle Identification at High Energies, JINR-Report D13-9164, Dubna (1975); *Nucl. Instr. Meth.* **127** (1975) 525–45
[165] A.S. Glassner, Surface Physics for Ray Tracing, in A.S. Glassner (ed.), *Introduction to Ray Tracing*, Academic Press, New York (1989) 121–60